Diplomarbeit
Master Thesis

VUV spectrograph - Characterization and Optimization

ausgeführt am Atominstitut der Fakultät für Physik der TU Wien
zur Erlangung des akademischen Grades Diplom-Ingenieur
im Rahmen des Studiums 066 461 Technische Physik

betreut durch

Univ.Prof. Dipl.-Phys. Dr.rer.nat. Thorsten Schumm

und unter Mitwirkung von

Tomas Sikorsky, PhD,
DI Fabian Schaden,
Kjeld Beeks, PhD

eingereicht von

Felix Schneider, BSc
Matrikelnummer 01527147

Wien, 13. Juli 2022

Unterschrift (Verfasser) Unterschrift (Betreuer)

Die approbierte gedruckte Originalversion dieser Diplomarbeit ist an der TU Wien Bibliothek verfügbar
The approved original version of this thesis is available in print at TU Wien Bibliothek.

Zusammenfassung

Ein Spektrograph für den Wellenlängenbereich von etwa 120 nm bis 200 nm wird anhand zweier verschiedener Sensoren charakterisiert: einer basierend auf einem Charge-Coupled Device, sowie einer basierend auf einer Kombination aus Micro-Channel Plate, Leuchtschirm und Complementary Metal-Oxide Semiconductor Bildsensor. Zur Kalibrierung wird das Spektrum eines Excimers aufgenommen und analysiert. Daraus ergibt sich eine Wellenlängendichte von 0.0032 nm/mm in der Fokusebene. Ebenso wird das Spektrum einer Deuterium-Bogenlampe aufgenommen. Verschiedene Kontroll- und Datenanalyseprogramme werden entwickelt und getestet, und verschiedene Kombinationen aus Micro-Channel Plate- und Leuchtstoff-Versorgungsspannungen werden sowohl mit als auch ohne Signal vermessen und das Signal-Rausch-Verhältnis verglichen.

Des Weiteren werden drei Versuche zum Bau einer kompakten Vakuum-Ultraviolett-Lichtquelle mit niedriger Intensität und hoher Genauigkeit durchgeführt, bei der schließlich das Excimer-Spektrum von Xenon angeregt durch einen Alpha-Emitter gemessen wird.

Zusätzlich werden zwei neue Funktionen in das bestehende Transmissionsmessgerät für den Vakuum-Ultravioletten Wellenlängenbereich implementiert, die sowohl Wiederholbarkeit als auch Messgeschwindigkeit verbessern.

Abstract

A spectrograph operating in the wavelength range of 120 nm to 200 nm is installed. Two different light detectors for the spectrograph are characterized, the first one using a Charged-Coupled Device as image sensor, and the second one using a combination of Micro-Channel Plate, phosphor screen and Complementary Metal-Oxide Semiconductor image sensor. Spectra of an excimer lamp are obtained and used for calibration, leading to a wavelength density on the focal plane of 0.0032 nm/mm. Spectra of a deuterium arc lamp are also taken. Different control and data analysis tools are developed and tested, and different supply voltages of the Micro-Channel Plate and phosphor screen are measured in both signal and dark situations, and the signal-to-noise ratio compared.

Furthermore, three attempts at creating a compact low-intensity, high-precision calibration source for vacuum-ultraviolet light are performed, resulting in the measurement of a Xenon excimer spectrum generated by an alpha source.

Additionally, two new features for a transmission measurement setup operating in the Vacuum Ultraviolet wavelength range are developed, enhancing repeatability and measurement speed.

Acknowledgements

Arguably, this thesis represents a personal milestone, standing at the crossroads after many years of studying. And getting there, working in the group, certainly was an adventure of its own which I enjoyed very much thanks to a few very special people. I owe much gratitude to Thorsten Schumm who steered our work gently, wisely and with smart questions while at the same time binding the team together with the attractive force of cake at group meetings. Just as much, I deeply appreciate the fruitful discussions with and constant support from Tomas Sikorsky, Kjeld Beeks and the rest of the group. I would also like to thank Fabian Schaden for his excellent guidance, helpful hints and his faith in my work.

I would not be where I am now without my brothers, my parents or my grandparents and their dogs, and I am thankful for that. Finally, and most importantly, I would like to thank my wife, Bianca, who has helped and supported me in every possible way, with soothing words when things wouldn't go well or by sharing my joy when they at some point would.

Die approbierte gedruckte Originalversion dieser Diplomarbeit ist an der TU Wien Bibliothek verfügbar
The approved original version of this thesis is available in print at TU Wien Bibliothek.

Contents

Die approbierte gedruckte Originalversion dieser Diplomarbeit ist an der TU Wien Bibliothek verfügbar
The approved original version of this thesis is available in print at TU Wien Bibliothek.

1 Introduction

Time as a concept is familiar to all of us. The measurement of time is nothing new, either. A vast variety of mechanisms, from candles burning at a constant rate to the predictable turns of the sun over the sky to the periodic oscillation of a quartz crystal, has been used to find and measure temporal distances.

The recent developments in the area of time measurement focus on size and accuracy [4, 31]. Currently, the ultima ratio of measuring time are atomic clocks [4]. By measuring time using the precise energy of an electronic transition as frequency standard, such clocks achieve high precision at the cost of increased complexity and high instability against changes in the electronic environment. This trade-off can be reduced by the use of nuclear transitions, particularly due to their higher stability against environmental changes. Light emitted from such transitions is usually highly energetic and commonly referred to as γ radiation. To be technically viable with today's technology, the transition energy needs to be low enough to reach the optical spectrum. Currently, only one such nuclear state transition with low enough energy is known: it is that of the thorium isomer ^{229m}Th to its ground state, ^{229}Th.

To make matters more difficult, this transition energy is not yet well-known. The most precise measurements in literature place it around 8.2 eV, but a much more precise knowledge is needed for an actual clock [39]. This information can then be used to construct a laser which can be locked-in on the transition. One approach to finding this energy is, simply put, exciting the nucleus and then measuring the energy of the emitted photon. As it turns out, this is a complex undertaking, even more so when the nucleus is surrounded by other atoms, e.g. when it is embedded into a crystal. The transition energy is in the same regime as electronic transitions so that - depending on the band gap - photons emitted from such transitions can be absorbed by electrons and may never be seen outside the crystal. Furthermore, internal conversion can occur if the band gap is smaller than the isomer transition energy [44].

Exciting the nucleus, that is, generating the ^{229m}Th state, is also not trivial. One commonly taken approach involves the α-decay of ^{233}U to ^{229}Th. It is well-known that the population efficiency achieved with this method is very small, with around 2% decaying to the isomeric state [5]. To complicate things further, the α-decay deposits considerable recoil energy on the newly created thorium nucleus which increases the chance of it ending up in an unfavorable chemical environment [42]. Such an environment increases the change for any excited state to decay via internal conversion without emitting the characteristic photon.

But there is another way of creating ^{229}Th both in its ground and isomeric state via radioactive decay. This decay chain involves the β-decay from ^{229}Ac to ^{229}Th. This decay populates the isomeric state with at least 14%, compared to around 2% population efficiency of the α-decay of ^{233}U. The recoil is very small as well, with around 2 eV compared to 84 keV for the α-decay, and should leave the thorium nucleus at its place in the crystal. Considering these factors, detection of the characteristic photon should be much more likely [44].

However, this approach is not without obstacles itself. ^{229}Ac has a low half-life of only 62.7 min so it needs to be created just before the experiment [40, 44]. If one follows the decay chain, one will see that this is doable. ^{228}Ra can be neutron-activated to become ^{229}Ra which in turn will decay into the desired ^{229}Ac via β-decay. One does need the right tools for it, though. And here at the Atominstitut in Vienna, we have them: skilled chemists for material preparation, a suitable crystal growing machine, a reactor for neutron activation and a measurement setup for vacuum ultraviolet (VUV) photon detection.

Now, this master thesis focuses on buildup and calibration of the measurement setup needed to detect these photons from the decay of ^{229m}Th into its ground state after having been produced from ^{229}Ac decay in a crystal.

Die approbierte gedruckte Originalversion dieser Diplomarbeit ist an der TU Wien Bibliothek verfügbar
The approved original version of this thesis is available in print at TU Wien Bibliothek.
TU Bibliothek Your knowledge hub WIEN

2 Theoretical background

In order to understand the experiment setup, some theoretical foundations are presented here. Knowledge of the properties of the CaF_2 crystals used in the experiment and the inner workings of the measurement setup are crucial to a successful experiment.

2.1 Th:CaF_2 crystals

At the center of attention is, of course, Thorium. It needs to be created and transported to the spectrometer in a suitable container. Other experiments have used ion traps to store such atoms. These are not suitable for our needs in this experiment as the ^{229}Ac needs to be produced shortly before the experiment by neutron capture in the reactor and then quickly transferred to the spectrometer.

If doable, it is much more beneficial to embed thorium nuclei into a crystal. This way, the chemical surrounding can be precisely controlled. At the same time, handling is easier and the density of Th nuclei is much greater than traditional methods with well-defined surroundings like optical lattices or ion traps.

When the Actinium approach to measuring the isomeric state was first proposed, the ^{229}Ac was to be implanted into crystals with good transmission characteristics around 150 nm, where it would then decay into ^{229m}Th [44]. Implantation however leaves the electronic surroundings in an undefined state, potentially opening the internal conversion decay channel for ^{229m}Th decay without the emission of a characteristic photon in the VUV range. By doping the crystal during growth, the electronic surrounding can be controlled much better, ideally inhibiting the internal conversion decay channel.

The thorium isomer transition energy is known to be in the vicinity of 8.1 eV [39]. Any crystal used for Th doping therefore needs to have a higher band gap to allow such light to pass through. Furthermore, a simple structure facilitates numerical calculations which in turn help understand the chemical surrounding of the dopant. Calcium fluoride fulfills these requirements, having a simple and well-understood cubic face-centered lattice [45], and a band gap of 11.8 eV [36]. Due to an exciton excitation at 11.2 eV, the effective transmission in CaF_2 is reduced to 9.8 eV [2]. Another candidate crystal with a sufficiently high band gap is MgF_2.

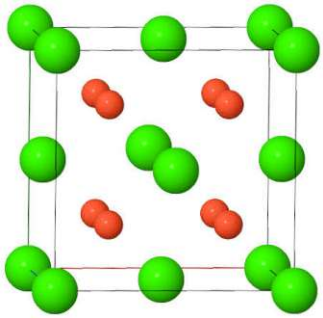

Figure 1: Face centered cubic unit cell of CaF_2 with F^- as orange spheres and Ca^{2+} ions as green spheres. [45]

In the lattice, Ca^{2+} takes the position at 000 whereas the two F^- sit at $\frac{1}{4}\frac{1}{4}\frac{1}{4}$ and $\frac{3}{4}\frac{3}{4}\frac{3}{4}$, as shown in Figure 1. As can be seen, each Ca cation is compensated by two F anions. When Th is doped into the crystal, it is most likely to take the Th^{4+} configuration and replace Ca^{2+} in the lattice [2].

Since this configuration requires two extra negative charges to be bound, charge compensation occurs. Various mechanisms are possible here. Density functional theory (DFT) calculations show that interstitial fluorides are most likely but contaminations with oxygen or sodium can also serve as compensation charges if present during crystal growth [21].

First experiments have produced ^{229}Th:CaF_2 crystals with poor transmission in the VUV range. The most probable explanation for this phenomenon is the loss of fluoride during growth. The result is a fluoride deficient crystal with many defects, possibly metallic Ca colloids and possibly thorium in its Th^{3+} configuration. It was found that providing additional fluoride to the crystal greatly improves

Die approbierte gedruckte Originalversion dieser Diplomarbeit ist an der TU Wien Bibliothek verfügbar
The approved original version of this thesis is available in print at TU Wien Bibliothek.

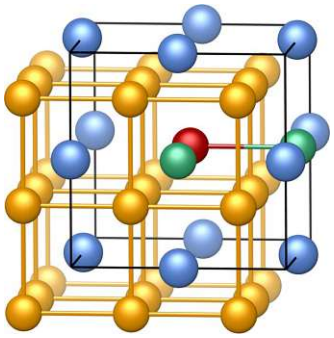

Figure 2: CaF_2 with Th dopant in the most favorable charge compensation state. Ca^{2+} blue, F^- yellow, Th^{4+} red, charge compensating F^- green. Taken from [21].

its VUV transmission [2]. Transmission was even worse for ^{229}Th doped crystals compared to ^{232}Th doped ones. Since the only difference relevant in the crystallographic environment is the presence of α-decays, one can conclude that the loss of fluoride is amplified by the the violent decay of ^{229}Th to ^{225}Ra.

To this end, high-transmission CaF_2 crystals with various dopants can be produced by the group. Building on these foundations, the production of a ^{228}Ra doped CaF_2 crystal with good transmission properties for use in the envisioned experiment is now viable.

2.2 VUV Spectrometers

As this thesis focuses on building and calibrating a spectrometer working in the VUV range, understanding the ins and outs of such a device is crucial for mission success.

A spectrometer is any device capable of measuring intensities of spectral bands of light, most often using a dispersive element to separate different wavelengths spatially. [6]. The resulting information will consist of the relative intensities of light at different wavelengths, also known as spectrum.

Light spectra can reveal plenty of information about the sample. Depending on the energy scale of the light, different properties can be probed, ranging from chemical bonds to the concentration of specific elements, or in cases such as ^{232}Th, even nuclei.

Optical spectrometers are conceptually simple devices consisting of only two components: a spectral apparatus and a detector. If a camera or a two-dimensional sensor is used as a detector, the device is more specifically referred to as spectrograph [6]. The spectral apparatus splits the incoming light into different wavelengths and the detector outputs information on the relative intensities. Of course, nothing is as easy as it looks and one needs plenty of additional parts to achieve the desired characteristics. One common addition are slits which at the input reduce the light effectively to a point source and at the output select a specific wavelength. As the spectral apparatus works using diffraction in most cases and is therefore dependent on the angle of the incident light, rotational stages are commonly employed for wavelength selection. And in the case of VUV that does not penetrate air [18], a vacuum chamber is needed as well.

Furthermore, spectrometers can be distinguished by their operating mode: sequential and simultaneous. Sequential spectrometers on one hand measure one wavelength at a time. In the case of VUV spectrometers, this is commonly achieved using photomultiplier tubes. Simultaneous spectrometers on the other hand have the capability of measuring the intensities of multiple wavelengths at once. This has benefits for example in situations where a time-dependence of the signal exists, as the spectrum is recorded practically instantaneous and no time drift needs to be considered.

A typical sequential spectrometer will employ two slits, one at the source and one in front of the detector. For a sequential spectrometer the second slit cannot be used. Instead, multiple wavelengths are projected onto a spatially resolving readout device such as a camera or a Micro Channel Plate (MCP) detector.

Spectrometers can also be classified according to the mounting of the spectral apparatus, or in other words, the principle of wavelength selection and focusing. Plenty of different tech-

Die approbierte gedruckte Originalversion dieser Diplomarbeit ist an der TU Wien Bibliothek verfügbar
The approved original version of this thesis is available in print at TU Wien Bibliothek.
TU Bibliothek Your knowledge hub WIEN

niques have been developed over the years, with the Seya-Namioka design being one of the most established ones in VUV spectroscopy [6]. It is especially popular because only the necessarily concave grating itself is turned around its own axis while entrance and exit do not move. Few, controllable moving parts is what one ideally wants in any vacuum environment, hence the advantage. However, this design typically suffers from astigmatism which can be corrected by using a corrected, aspheric grating [24].

The relation between wavelength λ and rotation angle of the grating θ in a Seya-Namioka-type monochromator is given by

$$\lambda = \frac{2\sigma}{m} \cos K \sin \theta \tag{1}$$

where σ is the grating constant, m the spectral order, $2K$ the angle between incident and exiting rays and θ is the angle of grating rotation measured from the bisector of $2K$ [24]. The same design can also be used as a simultaneous spectrometer. In this case, an aberration corrected grating must be used, with the side effect that the focal plane does not lie in the normal of the light path but about 30° from it [30]. A schematic drawing of a Seya-Namioka type simultaneous spectrometer including the angles K and θ is given in figure 3. The spectrometer used in this work is also of the aberration corrected Seya-Namioka type.

In the far-field approximation the wavelength resolution is determined by both the wavelength divergence given in equation (1) and the diffraction divergence stemming from the limited size of the wave front. The latter factor can be expressed approximately as

$$\Delta\theta \approx \frac{\lambda}{L \cos \theta} \tag{2}$$

with L being the size of the illuminated area on the grating [43]. Combining equation (2) with $\Delta\lambda = \frac{2\sigma}{m} \cos(K) \cos(\theta) \Delta\theta$ obtained from equation (1), we get an expression for the approximate resolution of a diffraction grating in the Seya-Namioka configuration,

$$\frac{\Delta\lambda}{\lambda} = \frac{2\sigma}{mL} \cos K. \tag{3}$$

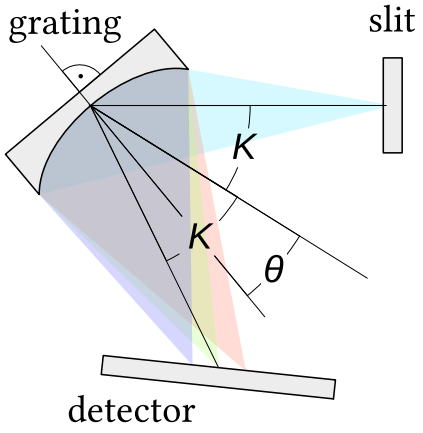

Figure 3: Schematic drawing of a spectrograph following the Seya-Namioka design. The angle K is constant, whereas the angle θ can be modified to select different wavelengths.

One can easily see that not illuminating the entire area of the grating can limit resolution, and that increasing grating size will increase resolution. Another way to improve resolution would be to use a higher order of diffraction with the additional risk of overlaps with lower orders.

At the end of the day, the resolution of the system is also determined by the detectors. Technologies used in the detectors in this work are presented next.

2.3 Charge-Coupled Devices

The spectrometer used in this work produces a focal plane where multiple wavelengths are in focus on different positions. This necessitates the use of a spatially resolving detector with a grid of pixels, the values of which can be determined individually. One such technology available is the CCD, or charged-coupled device. It resembles a coupled chain of capacitors, each of which can transfer its charge to the neighbor. A readout circuit can then transfer charges to the side and read them out sequentially. Even though Complementary Metal-Oxide Semiconductor (CMOS) sensors, discussed later in section 2.5, nowadays took over the role of image sensing in consumer products, CCD sensors are

Die approbierte gedruckte Originalversion dieser Diplomarbeit ist an der TU Wien Bibliothek verfügbar
The approved original version of this thesis is available in print at TU Wien Bibliothek.
TU Bibliothek Your knowledge hub WIEN

still used for high-end scientific applications due to their performance in low-light conditions.

2.3.1 Working principle

Each pixel is essentially a metal-oxide semiconductor (MOS) capacitor, exposed to light. Charge generation happens via the photoelectric effect. Therefore the photon energy needs to be greater than the band gap of the material used, $E_\lambda > E_{\text{band gap}}$. For silicon with a band gap of $E_{\text{band gap}} = 1.1\,\text{eV}$, this translates to wavelengths shorter than $1.12\,\mu\text{m}$ [26]. Silicon detectors are therefore generally suited for light in the visible and ultraviolet (UV) range, and with some effort can be used in the VUV and even soft X-ray regime, too.

Single pixels act as potential wells, filling up with charge generated by the photoelectric effect or dark signal. Typically dark signal stems from thermal noise and cooling is required for exposures more than a few seconds long.

A readout circuit will then generate voltage specific sequences which shift the charge row by row into the serial register. For readout, each row of the serial register is then shifted towards the output where charge is converted into voltage pulses. From the timing of those pulses, the 2D image is reconstructed. In more complex sensors, multiple serial registers and output amplifiers might be present, each assigned to a different region of the sensor. During readout, both horizontal and vertical binning can already be performed, where charges of multiple pixels are collected as one. This charge summation does not introduce readout noise and is therefore sometimes also called "noiseless co-addition". A diagram of a CCD and the readout directions is shown in figure 4.

This readout sequence takes time which is why some systems employ shutters and thereby prevent new signal distorting data during readout. Another way to prevent data from accumulating during readout is by using another pixel array with an opaque mask, usually termed "frame store area". Charges can then be shifted very fast, and readout can take much more

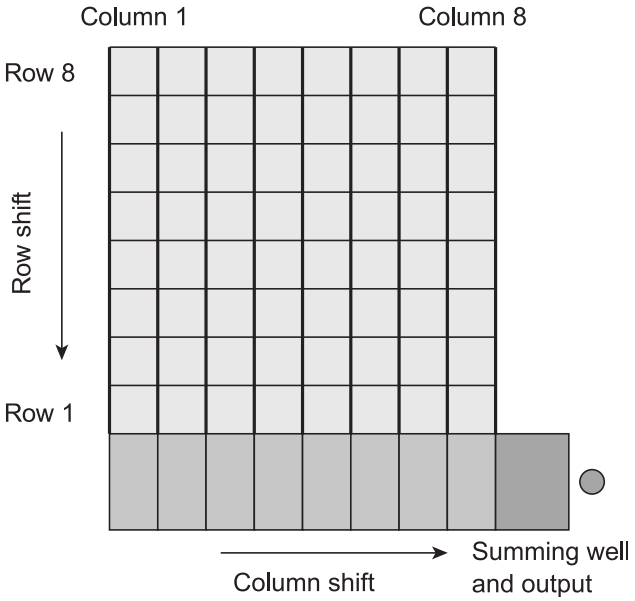

Figure 4: Schematic drawing of a CCD sensor. At readout, row by row is shifted into the serial register, depicted as the bottom row. There, the charges are shifted towards the output where charge to voltage conversion takes places. The spatial information of the image is then reconstructed from the timing of the output signal. Graphic taken from [26]

Die approbierte gedruckte Originalversion dieser Diplomarbeit ist an der TU Wien Bibliothek verfügbar
The approved original version of this thesis is available in print at TU Wien Bibliothek.

time. The systems used in this work however do not employ such methods, so readout rates have to be carefully considered and accounted for.

A key part of the readout is the conversion of charge to voltage, following the equation

$$V = \frac{Nq}{C} \tag{4}$$

with q being the electronic charge, C being the capacitance of the node where the conversion takes place and N the number of electrons accumulated. Typical voltages produced by a single electron range between 1 and 50 µV [26]. This voltage is usually buffered by a MOSFET (metal oxide semiconductor field-effect transistor), transferred off-chip, amplified and converted to a digital signal. This MOSFET needs to be reset before each readout so values don't accumulate.

A key differentiation is the CCDs illumination mode. On front-illuminated CCDs the light falls directly on the gate structure. This structure absorbs most of the light below 400 nm, and produces complex interferences between different process layers. They are however much cheaper than back-illuminated chips. For scientific and high-end applications, almost exclusively backside illuminated chips are used. These need to be post-processed after fabrication, adding to the cost. Since the silicon is directly illuminated, they usually have good quantum efficiency over a large spectral range. The CCD chips employed in both Andor cameras used in this work are backside illuminated.

Backside illuminated CCDs are usually limited by reflections on the surface and the ability of the silicon to absorb photons. The latter is a function of temperature and layer thickness. Layer thickness is by itself a difficult topic. Thinner layers ease the diffusion of the electrons to the front side pixels where they are collected. At the same time, thin layers also introduce interference fringing from multiple reflections within the CCD. To improve reflective properties of the CCD, anti-reflectance (AR) coatings are applied.

2.3.2 Noise characteristics

Now that we know what a CCD is and how it works we can move forward and discuss its noise characteristics.

The most fundamental uncertainty in the output of the CCD is the read noise. While typically measured in electrons rms, it occurs at the charge-to-voltage conversion and is actually a voltage uncertainty [26]. After resetting the output node, its value is uncertain. To limit readout noise, most high-end CCDs read voltage once before and once after charge transfer and only take this difference. This technique is called correlated doubled sampling, or CDS.

Read noise can be characterized by calculating the standard deviation of an entirely dark frame with practically zero exposure time, often referred to as zero or bias frame.

Another effect significantly contributing to noise is dark signal, also termed dark current. It is a thermal factor, and governed by the equation

$$D = 2.5 \cdot 10^{15} \cdot A_{\text{pix}} D_{\text{FM}} T^{1.5} e^{\frac{-E_g}{2kT}}. \tag{5}$$

D refers to the dark signal in generated electrons per second, A_{pix} is the area of the pixel, D_{FM} a quality parameter of silicon, given in nA/cm^2, k is the Boltzmann constant, E_g is the band gap of silicon and T the temperature [26].

Dark current can be characterized by taking multiple exposures without signal, adding them together. Usually, median filtering or clipping is employed to reject cosmic rays. These methods work well at room temperature. When cooled however, this type of noise reaches the same order of magnitude as read noise and these measurements become inaccurate and complicated. Furthermore, spatial variations of the dark current are possible due to inhomogeneities of the silicon. Furthermore, such measurements also tend to include other types of noise such as light leaks from the vacuum vessel or glow from detector diode breakdown.

Dark noise refers to the variations in the dark current.

Die approbierte gedruckte Originalversion dieser Diplomarbeit ist an der TU Wien Bibliothek verfügbar
The approved original version of this thesis is available in print at TU Wien Bibliothek.

Another source of noise is so-called fixed pattern noise which is mainly due to sensitivity fluctuations from pixel to pixel. If one has access to a uniformly illuminated image, one can perform "flat field correction" and divide the signal image by that.

2.4 Micro channel plate detectors

Direct imaging technologies such as CCDs and CMOS image sensors are not suitable to detect single photons. Their noise characteristics are too high to allow for differentiation between individual photons, even when cooled. In situations where single photons need to be detected, photomultiplier tubes (PMTs) usually are the tool of choice as they provide huge gain factors while at the same time producing so little noise that they even need not be cooled. However, they do not provide spatial resolution as is needed for a spectrograph like the one discussed in this thesis.

Here, the micro channel plate (MCP) detector comes into place. It can perform similarly well as the traditional PMT while at the same time providing spatial resolution. To achieve such a feat, MCPs are essentially glass plates with a great number of miniaturized photomultiplier tubes built in. This works by building capillaries, also referred to as channels, in parallel under a specified angle. The inner surface of these channels is coated to have proper electrical resistance and secondary emissive properties. Typical diameters range from 6 µm to 25 µm [21].

Once a primary electron hits the inner wall of such a tube, some secondary electrons are emitted. As with PMTs, a high voltage is applied across the MCP so secondary electrons are accelerated towards the other side, releasing more electrons when they hit. That way, an electron avalanche is formed and released on the other side of the detector. The actual amplification is heavily dependent on a multitude of parameters [8]. A schematic drawing of this process is given in figure 5. And because each tube is so small, high spatial resolution

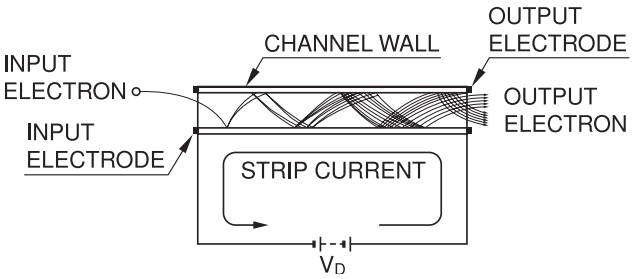

Figure 5: Schematic diagram of the electron amplification process in an MCP. An input electron, also called primary electron, hits the channel wall and generates more than one secondary electrons. Because of the high voltage, these are accelerated towards the other side of the wall, generating even more secondary electrons. The result is a pulse of output electrons that can be measured. Graphic taken from [21].

can be obtained.

The actual photon to electron conversion is facilitated by coating the surface appropriately, in the case of VUV, usually with CsI [20].

The gain of such an MCP can be modeled after a PMT with a specific number of dynodes and increases with applied voltage V, following the formula

$$G = \gamma \left(\frac{nV_{pk} + V}{nV_c} \right)^k \left(\frac{V}{nV_c} \right)^{k(n-1)}, \quad (6)$$

with γ the effective electron acceptance area ratio, eV_{pk} the input energy of the photoelectrons, V_c the minimum potential for a secondary emission ratio of one, and n the characteristic number of dynodes [9]. Over an extended period of use, channel saturation effects occur and the assumption of a constant E field in the tube breaks down and channel gain shows more complex behavior.

Looking closely at equation (6), one can see that the energy of the incoming photoelectron eV_{pk} also determines the gain and, as a result, the peak height of the output pulse. This is especially relevant for high-energy photoelectrons. In the case of VUV light, typical photon

Die approbierte gedruckte Originalversion dieser Diplomarbeit ist an der TU Wien Bibliothek verfügbar
The approved original version of this thesis is available in print at TU Wien Bibliothek.
TU Bibliothek Your knowledge hub WIEN

energies are in the range of 10 eV and therefore contribute only marginally to the gain. This means however that pulses with much greater height than possible by just a VUV photon could be disregarded as background. For such a scheme to work, reliable detection of pulse height needs to be possible.

To generate even higher gains, MCPs can be stacked together. It is not uncommon to see assemblies of two or three MCPs. In such assemblies, a small enough space between the plates is necessary to avoid the spread of signal to adjacent channels on the plate interfaces. Distances between plates of 10 µm can be achieved and counter this unwanted side effect to some extent [29].

MCPs only have a finite lifetime as channel saturation effects take place and degrade the gain of the system. Lifetime is usually measured as accumulated output charge in C/cm^2, with a typical lifetime of around $1\,C/cm^2$ for newer devices [29].

2.4.1 Noise characteristics

Dark count rates of 0.1 to $1.3\,cm^{-2}s^{-1}$ are common on MCP detectors [12, 19]. Only a negligible part of that can be attributed to cosmic rays. Operating temperature also has no measurable impact on dark count rates. Field emissions from channel defects have been reported in the past but without conclusive results. If present, radioactive decay of elements inside the MCP can be a significant factor for noise. In literature, noise was previously not found to be dependent on the supply voltage [12].

Time-dependent noise also occurs and can be attributed to outgassing of the detector. Part of this effect can be attributed to water vapor and oxygen being released from the large surface area, especially if the MCP was exposed to air before, and the other part is outgassing by the glass material itself. The time-dependence of this effect was observed under constant high voltage and literature suggests that the decay of this type of noise would be slower if not under constant high voltage because the electron scrubbing effect would be missing [12].

Outgassing can be countered by bake-out of the detector, as well as operation for several hours to days under high voltage and high vacuum.

2.4.2 Phosphor screen

Various readout modes for MCPs are possible, providing different quantities for further processing. Commonly used are multichannel analyzers, which can precisely distinguish and count charges, resulting in pulse height distributions (PHD) but cannot resolve spatially [12].

For spatial resolution, phosphor screens are used which convert the electron pulse to back to photons in the visible light region. Phosphor screens do not actually contain phosphor but instead use different combinations of materials to achieve the required luminescent properties. These materials have standardized names and come with different central emission wavelengths, decay times and grain sizes. For the MCP, materials with fast decay times and small grain sizes are reasonable. Typical grain sizes used in production are in the order of 1 to 3 µm [14, 17].

Often, phosphor screens are coated with a thin Aluminum layer to reflect emitted light towards the desired direction. Furthermore, some screens are coated with indium tin oxide (ITO) to avoid electrostatic effects [14].

The physical process of luminescence by electron beams is called cathodoluminescence and well-known in cathode-ray tubes. Not all electrons hitting the screen penetrate the surface and contribute to luminescence. A part is deflected by elastic scattering, and a usually much smaller deflected part by inelastic scattering, combined giving the back-scattering factor η_0. This factor depends only weakly on the incident electron energy but rather on the number of electrons per molecule, $\eta_0 = \frac{1}{6} \ln Z_m - \frac{1}{4}$ [38].

Once an electron enters the phosphor solid, it follows the Bethe Bloch equation, losing more energy as it slows down. Most energy is dissi-

Die approbierte gedruckte Originalversion dieser Diplomarbeit ist an der TU Wien Bibliothek verfügbar
The approved original version of this thesis is available in print at TU Wien Bibliothek.
TU Bibliothek Your knowledge hub WIEN

pated through ionization processes, producing secondary electrons. Secondary electrons are often energetic enough to ionize as well, resulting in secondary electron multiplication. The average energy required to create an electron-hole pair near the band edges is another important parameter in cathodoluminescence efficiency. Energy from thermalized electrons, that is free electrons near the band edge, is then transferred to the luminescence centers via molecular energy levels in the case of complex inorganic compounds [38]. Other phosphor materials can have different mechanism of energy transport.

The total efficiency of a P46 phosphor material is in the order of $\eta = 95$ photons per electron [41].

The photons emitted from the phosphor screen can then be collected by a image sensor, which is in the case of this work a CMOS sensor.

2.5 Complementary metal-oxide-semiconductor image sensors

While CCD sensors, discussed in section 2.3, dominated the market for image sensors for many years, another technology has taken over much of the market nowadays: complementary meta-oxide-semiconductor (CMOS) image sensors.

Such a sensor consists of an array of light-sensitive pixels. Each pixel has its very own photodiode and transistors for performing charge-to-voltage conversion. Several routing layers are required underneath the transistors to transport the signals to the control circuit. This is already in contrast to CCD sensors where no charge is passed from capacitor to capacitor during readout and no complicated routing is required underneath the light sensitive region.

Only in recent years, backside illumination of CMOS image sensors was developed and rolled out in large scale. Not just the performance in low light situation is improved in backside illuminated CMOS sensors, but they also enable better anti-reflecting coatings and smaller pixel sizes [25]. The sensor used in this work uses backside illumination. A simplified schematic drawing of a monochrome backside illuminated CMOS image sensor's light sensitive region is given in figure 6.

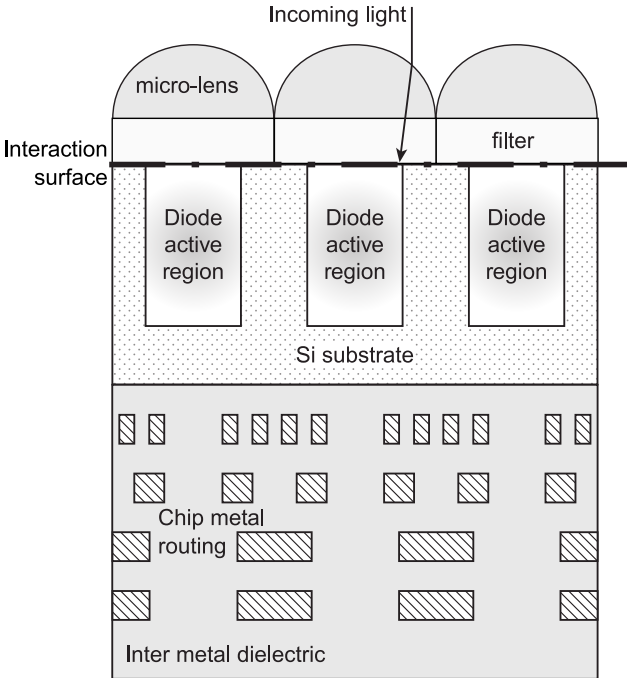

Figure 6: Schematic drawing of a backside illuminated CMOS image sensor. Light falls in from the backside, focused on the active region in the silicon substrate with micro-lenses. Underneath, some space for additional transistors and routing is required. Graphic taken from [25]

On a CMOS sensor, the signal chain starts with a photodiode. The current generated by it generally consists of thermally generated leakage or dark current and the signal introduced by photons,

$$I_{\mathrm{PD}} = I_{\mathrm{dark}} + Q_D G_A A_D G_L L_O \qquad (7)$$

with I_{PD} the output current of the photodiode (PD), I_{dark} the dark current, Q_D the quantum efficiency of the photodiode's material, G_A the gain factor of the photodiode area compared to the total pixel area, A_D the area of the

Die approbierte gedruckte Originalversion dieser Diplomarbeit ist an der TU Wien Bibliothek verfügbar
The approved original version of this thesis is available in print at TU Wien Bibliothek.
TU Bibliothek Your knowledge hub WIEN

photodiode, G_L the gain of the optical assembly including microlenses and, finally, L_O the input intensity [7].

The dark current I_{dark} depends on the photodiode's area and geometry, as well as temperature. Any variation in its area will therefore immediately result in a fixed pattern noise over the chip. These variations are usually termed dark current non-uniformity, or DCNU. In general, fixed pattern noise will increase with increasing temperature [7].

For an exposure, the diode is first reset. Then, the diode capacitance is slowly discharged by the current introduced by the signal and dark current. Once the exposure time is over, pixel voltage is read out using some transistors. These readout steps add flicker noise and thermal noise. The voltage is then passed towards the analog-to-digital converter where additional noise is introduced.

As in CCDs, the reset noise is one of the major sources of noise. It is usually compensated for by using correlated double sampling (CDS), using a second, buried photodiode with a capacitance large enough to store the reset value. The reset value can then later be subtracted [7].

Like a CCD sensor, CMOS sensors are also usually read out line-by-line. If fast enough, this usually poses no problem for image quality and a rolling shutter, that is, continuous exposure, is used. In fast-moving scenes this is unsuitable and will lead to distortions in the image. The camera used in this thesis also uses a rolling shutter design.

In most modern CMOS sensors, various measures to minimize noise in different parts of the readout chain are taken, such as the introduction of intermediate column amplifiers. The full readout chain then might look similar to the one depicted in figure 7. This more complex readout chain results in lower read noise when operated under higher gain of the output amplifier [23]. A representative read noise to gain curve is given in figure 8. Increasing the gain value has some other effects beside noise, too. The full-well capacity decreases

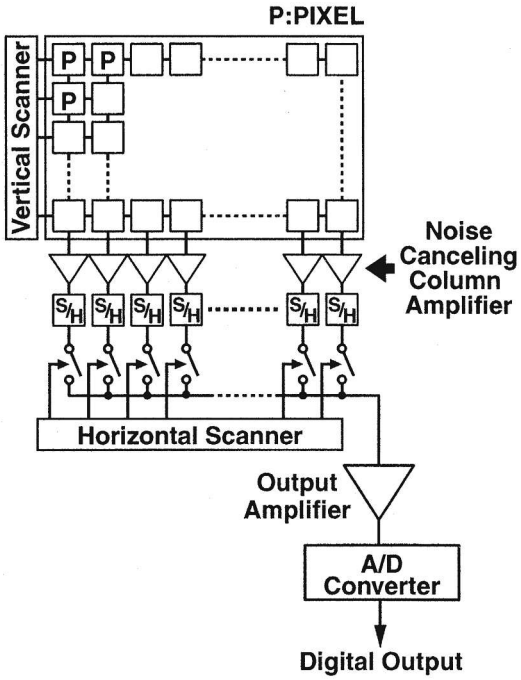

Figure 7: Diagram of the readout stages of a CMOS chip. Graphic taken from [23].

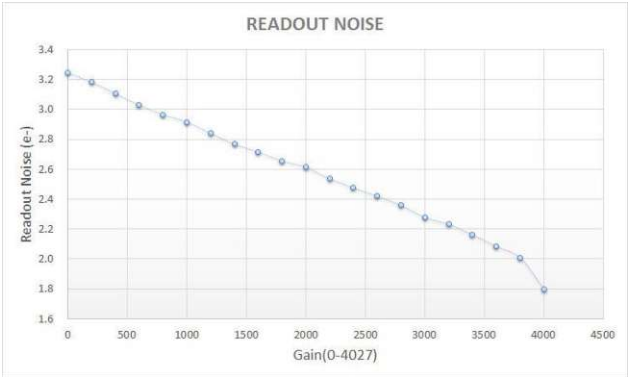

Figure 8: Read noise to gain curve for a QHYCCD QHY367C CMOS camera. Graphic taken from [35].

Die approbierte gedruckte Originalversion dieser Diplomarbeit ist an der TU Wien Bibliothek verfügbar
The approved original version of this thesis is available in print at TU Wien Bibliothek.
TU Bibliothek Your knowledge hub WIEN

so less electrons are required to saturate each pixel. At the same time, quantization error is reduced. Quantization error refers to the information loss stemming from the fact that most analog-to-digital converters (ADCs) only have 12 bit resolution and can therefore distinguish only 4096 values, whereas the full well capacity is often in the range of 15 000 electrons [35].

Besides gain, another parameter can be tuned on such CMOS sensors: the offset is used to shift values before conversion to a digital signal. Low values that would otherwise be clipped to zero can in this way be preserved. While not important in the use case of detecting bright dots, this technique is useful in astronomical imaging to prevent information loss [35].

In this work, a CMOS camera is used to detect dots on an MCP. For this use case, dark pixels do not carry relevant information and can be safely discarded, so the offset parameter is irrelevant. Gain however is relevant, as it defines the effective full-well depth and dynamic range. Gain values have to be chosen in such a way that dots on the MCP can be clearly distinguished from the background. At the same time, location information of the dots is crucial and a too high gain might negatively impact the ability to precisely locate the center of the dot.

3 Spectrometer with CCD camera

Let us recall what we aim to do. We are looking for a weak signal decaying in a matter of minutes, and we need to know the energy of the emitted photons as precisely as possible. So first of all, the system needs to be characterized and calibrated using sources with known wavelengths. This initial characterization is performed with an x-ray CCD detector installed, instead of an MCP detector, because it is much easier to handle and does not need to be kept under vacuum at all times. Additionally, MCP detectors are suitable for detecting single photons and easily overwhelmed with the comparatively powerful light sources at our disposal. The construction of a light source useful as reference for MCPs is discussed in section 5.

The setup as it was used for this part of the thesis consists of the H+P spectroscopy easyLIGHT apparatus [16] and a CCD camera. Initially, the device was delivered with a borrowed Andor iKon-M DO934P BN camera, until the ordered Andor Newton DO940P-BEN camera arrived. The Andor iKon-M DO934P BN camera has a sensor with 1024×1024 square pixels with a length of 13 µm [32]. The Andor Newton DO940P-BEN camera had a rectangular e2v CCD42-10 sensor with 2048×512 square pixels with a side length of 13.5 µm [27, 33]. This wide sensor allows covering a spectral range of about 100 nm at once.

The apparatus further includes a Xeryon ultrasonic rotation stage on which a Newport DGA-50 grating holder and, ultimately, the grating is mounted, controlled using a Xeryon XD-C actuator controller with serial number XD20052. The grating is specified to have a 1200 lines/mm groove density, 200 mm focal length, 64° deviation angle and a dispersion of 2.3 to 2.9 nm/mm. According to the supplied datasheet, wavelength resolution should be below 0.1 nm [15].

The entrance slit is a Thorlabs VA100C/M standard part with the set screw modified to use a long shaft and being installed outside the vacuum chamber. For connecting the camera to the grating chamber, a blue anodized adapter is used. The grating chamber is made out of steel. Both the grating chamber and the tube holding the slit are entirely coated in black paint which can be seen in figure 9.

3.1 Installation of the grating

Upon delivery, the grating was not yet mounted on the vacuum vessel. The grating was thus mounted following the instructions provided by the supplier [15].

A pinhole was installed on the port in front of the slit. An alignment laser was then installed

Die approbierte gedruckte Originalversion dieser Diplomarbeit ist an der TU Wien Bibliothek verfügbar
The approved original version of this thesis is available in print at TU Wien Bibliothek.
TU Bibliothek Your knowledge hub WIEN

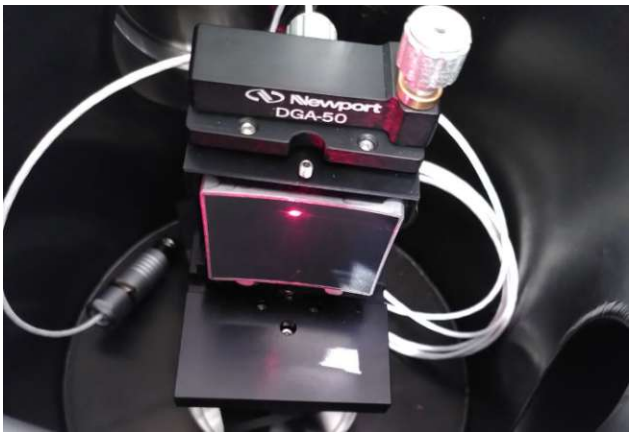

Figure 9: Grating installed in the spectrometer, with an unaligned laser pointing on it from the entrance slit. The black coating of the chamber is visible in the background.

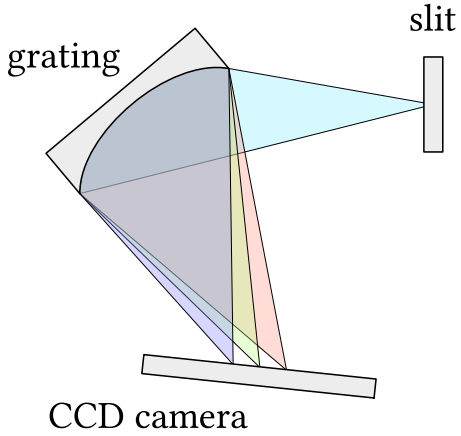

Figure 10: Schematic drawing of the spectrometer with the camera mounted. Light from a probe or light source falls through the slit on the grating. The wide CCD sensor of the Andor Newton DO940P directly detects the light, covering a spectral range of around 100 nm. The camera is mounted using an angling adapter so that multiple wavelengths are in focus at once. All components reside inside the vacuum vessel.

to point through the pinhole centered onto the slit. An image of the still unaligned laser on the grating is given in figure 9. The rotational stage was set to 0^{th} order. The grating was adjusted using the screws on the grating holder to point the laser exactly centered onto the output port. This procedure was difficult and had to be repeated multiple times as the rotation stage did not lock in position but wiggled around it when the screws were touched.

Once this crude alignment was done, a D_2 lamp with focusing mirror was connected to the system. First, the lamp was focused onto the slit, operating under air atmosphere. This was done as fast as possible to limit ozone production to a minimum. From there, the grating controller was turned to 1^{st} order and line width of the 121.5 nm D_2 line was minimized by turning the adjustment screws on the grating holder one half turn (π rad) at a time. With optimal position, a line width for the 121.5 nm line of 0.56 nm full width at half maximum (FWHM) is reached. This compares to 0.59 nm FWHM of the same line on the transmission measurement setup of the group which was improved in section 6.

This alignment does not directly guarantee that light sources directly placed on the slit will also produce the best possible image. This is because the mirror of the lamp does not produce a well-defined intensity distribution, so the central point in the light coming from the lamp cannot be identified. Furthermore, small misalignment of parts in the light path might lead to light entering the spectrometer under a slightly different angle, effectively shifting the spectrum as experience has shown.

3.2 Calibration using an excimer light source

An excimer light source works by ionizing noble gases which then form a very short lived molecule, a so-called “excimer”. Decay of the excimer then produces characteristic light in the VUV spectrum. In our case, an Excitech Elux 147 operating with Kr was used. This

Die approbierte gedruckte Originalversion dieser Diplomarbeit ist an der TU Wien Bibliothek verfügbar
The approved original version of this thesis is available in print at TU Wien Bibliothek.

light source provides a peak at 147 nm with a FWHM width of 10 nm, and some additional atomic lines from small contaminations [2, 13]. Contaminations are most likely to be Xe and C. Another distinctive feature that can be seen with this lamp is the rising edge of the spectrum, situated at the 123.5838 nm atomic line of Kr [1]. However, these features depend on the filling and can change if the filling is renewed.

The distinctive features of the spectrum can be used for characterization of the CCD chip, generating a relation between pixel index and wavelength. In the state the lamp was in at the time of the experiment, on October 4, 2021, the following features could be identified:

- the characteristic rising edge of the spectrum at 123.5838 nm;
- atomic lines from the Xe contamination at 117.0413 nm, 119.2037 nm, 129.5588 nm and 146.9610 nm;
- the Kr excimer peak at 147 nm with a FWHM of around 10 nm;
- and one C line at 165.692 821 nm.

These lines were identified from likelihood and experience, and by excluding other possibilities.

3.2.1 Andor iKon-M CCD with an 1:1 aspect ratio

Centering the iKon-M CCD camera on the central excimer peak, only wavelengths higher than 124.9 nm were visible. Therefore, the rising edge and the two lower Xe lines were unavailable for fitting. As location and width of the excimer peak are not as well characterized as the atomic lines and the central excimer wavelength, they were also not considered in the fit. The upper half of the image is unusable since the quadratic sensor covers more height than effectively illuminated by the grating. Alignment imperfections made it necessary to cut out a part of the image to improve resolution. For that reason, the width of the 147 nm peak

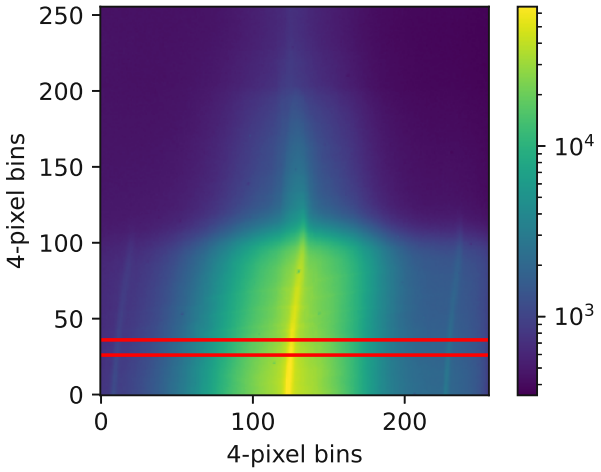

Figure 11: Pixel intensity data of the Excitech E-Lux 147 light source taken with an Andor iKon-M DO934P BN camera with 4x4 binning, in arbitrary units (a.u.). Intensity reduces in the upper half of the image as it is not properly illuminated by the grating anymore. An average over the slice between the two red lines was used for calculation of the spectrum.

of Xe was fitted for each row. A mean over the 10 rows with the lowest average peak width was finally calculated for further analysis, using the rows with indices 26 to 35. A binning of 4x4 pixels was applied, so one row is already the average over 4 pixel rows. The full image used is shown in figure 11 with the used rows for evaluation indicated by red lines.

Fits of linear and quadratic polynomials were compared. Both performed very well, achieving R^2 values higher than 0.9999. The quadratic fit was chosen in order to offset any nonlinearities in the system. A least-squares fit resulted in the polynomial

$$\omega(x) = c_0 + c_1 \cdot x + c_2 \cdot x^2 \tag{8}$$

with the coefficients

$$\begin{aligned} c_0 &= 167.4708\,\text{nm}, \\ c_1 &= -0.161\,406\,7\,\text{nm/bin}, \\ c_2 &= -2.1378 \cdot 10^{-5}\,\text{nm/bin}^2 \end{aligned} \tag{9}$$

Die approbierte gedruckte Originalversion dieser Diplomarbeit ist an der TU Wien Bibliothek verfügbar
The approved original version of this thesis is available in print at TU Wien Bibliothek.

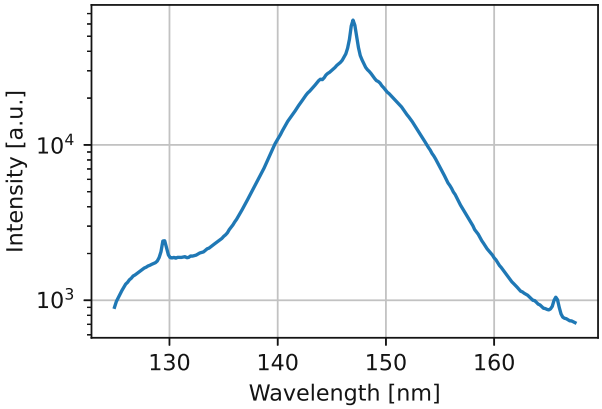

Figure 12: Spectrum of the Excitech E-Lux 147 light source, calibrated using a quadratic fit over the atomic lines of the contaminations. The peaks at 129.6 nm and at 147 nm are attributed to Xe whereas the peak at 165.7 nm is attributed to C. Visible as well is a broad Gaussian peak with a central wavelength at 146.7 nm and a FWHM of 9.8 nm.

The low value of c_2 as well as the good quality of the linear fit imply a very low degree of nonlinearities across wavelengths. The final spectrum obtained using this method is shown in figure 12.

Using this fit, the not-so-well measured quantities can now also be obtained and the central wavelength of the excimer spectrum is calculated to be 146.7 nm whereas the width (FWHM) of the peak evaluates to 9.8 nm.

Furthermore, the average spectral distance per pixel calculates to 0.0415 nm/px.

3.2.2 Andor Newton with a 4:1 aspect ratio

A similar measurement can be performed for the Andor Newton DO940P-BEN camera. As the sensor is much wider, this camera can cover a wavelength region of 89.8 nm in one image compared to 42.5 nm from the iKon-M model. When focused on the central 147 nm peak of the excimer spectrum, the entire VUV spectrum including all atomic lines and the rising edge are imaged at once. As before, the 166 nm Carbon line and the 147 nm and 130 nm Xenon lines are visible. Additionally the sharp edge of the excimer spectrum at 123.5838 nm and the Xe lines at 119.2037 nm and 117.0413 nm can be identified in the spectrum. The atomic lines as well as the sharp edge are used for fitting in this case, as they are very well known.

As before, the 147 nm Xe line was fitted for each pixel row and the 10 rows with the smallest width selected and averaged. The selected rows were those with indices 1 to 10. A 8-pixel binning was applied only on the vertical axis, so each row represents the mean over 8 pixel rows. Again linear and quadratic polynomials were fitted and their goodness compared. Both again showed very good R^2 values, the linear fit giving a value higher than 0.999 and the quadratic fit performing similarly well as with the iKon camera with a value higher than 0.9999. The least-squares fit of the quadratic polynomial (8) gave the coefficients

$$\begin{aligned} c_0 &= 195.8732\,\text{nm}, \\ c_1 &= -0.041\,269\,25\,\text{nm/px}, \\ c_2 &= -1.2655 \cdot 10^{-6}\,\text{nm/px}^2 \end{aligned} \tag{10}$$

Again, almost no nonlinearities in the spectrum can be found, even tough the chip covers around double the spectral range so any nonlinearities would be more visible. The final spectrum obtained using this method is shown in figure 13b.

Again, both central position of the excimer spectrum and FWHM can be measured by fitting a Gaussian and using the wavelength calibration obtained before. This gives a central peak at 145.8 nm and a FWHM of 10.2 nm. These values are in general agreement with both the former measurement on the iKon-M camera and the datasheet [2, 13].

Measuring the same peak on the McPherson spectrometer further discussed in section , one obtains a FWHM of 10.5nm, which also is in general accordance with the other values.

On average the calibration is determined to be 0.0438 nm/px. When taking into account

Die approbierte gedruckte Originalversion dieser Diplomarbeit ist an der TU Wien Bibliothek verfügbar
The approved original version of this thesis is available in print at TU Wien Bibliothek.

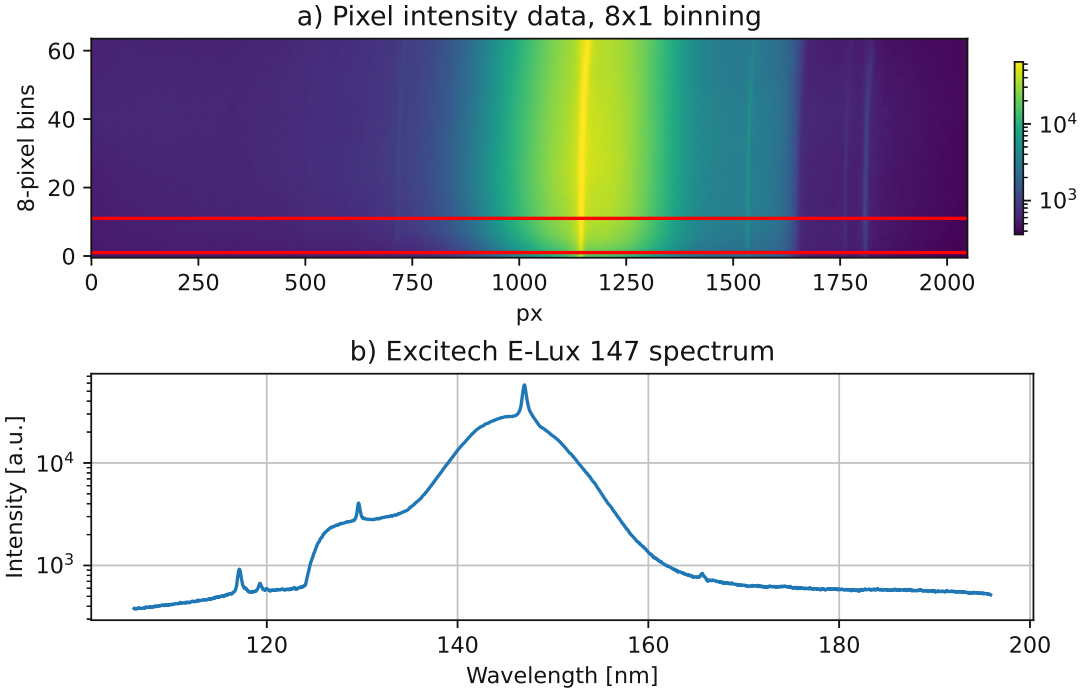

Figure 13: The raw pixel values (a), given in arbitrary units, are taken with an Andor Newton DO940P-BEN camera cooled to −64 °C with an exposure time of 10 s. A mean of the rows between the red bars was used for calculation of the spectrum. Xe and C peaks and the edge of the excimer spectrum were used in a fit of a quadratic polynomial for wavelength calibration.

Die approbierte gedruckte Originalversion dieser Diplomarbeit ist an der TU Wien Bibliothek verfügbar
The approved original version of this thesis is available in print at TU Wien Bibliothek.

the different pixel sizes of the two cameras, both measurements are in good agreement, yielding 0.0032 nm/mm.

3.3 D_2 lamp spectrum

While excimer lamps emit a broad spectrum, they are also difficult to manufacture and operate. A much more developed and easy-to-use light source in the VUV region is the D_2 arc lamp, short "D_2 lamp". It generates an arc in a Deuterium gas bulb that produces higher intensities in the VUV region than a similar H_2 arc lamp. The spectrum below 170 nm is dominated by a multitude of molecular lines overlapping to a seemingly continuous spectrum. In the case of this work, a Hamamatsu L11798 D_2 lamp was used, connected via a focusing mirror.

Focusing of the lamp proved difficult as the intensity profile after the mirror was nontrivial and hard to interpret. In the case of the iKon-M camera, a clear horizontal line was visible, depicted in figure 14. By adjusting the focusing mirror this line could also be moved in position. The most likely albeit not confirmed explanation would be that it is an artifact of the focusing mirror. Values close to it were not used in the calculation of the spectrum, instead the 100 rows with the highest resolution as determined by the width of the 121.5 nm peak were used. In this case, these had the indices 265 to 364.

For wavelength calibration, data from listing (9) were used, as well as the known wavelength of the atomic transition 121.53 nm [1] to calculate an offset. The resulting spectrum aligns very well with literature, showing both characteristic peaks between 120 nm and 130 nm as well as a trend of higher intensities towards the 160 nm region.

After installation of the Newton camera, no artifacts comparable to those shown in figure 14 could be detected. Both intensity and resolution were highest in the lowest part of the image. A strip of 50 pixel rows starting at the bottom was therefore selected for the calculation of the

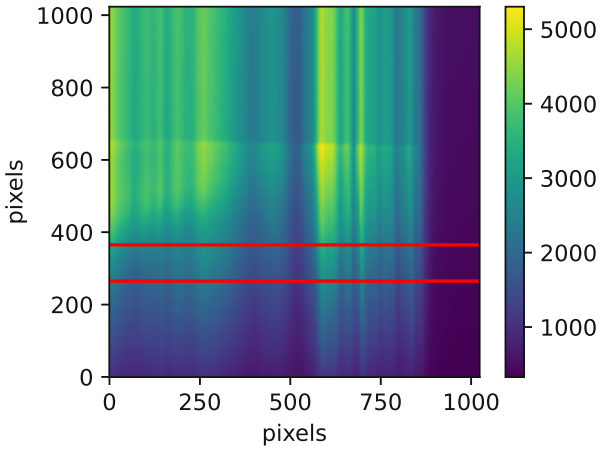

Figure 14: Unbinned pixel data of a D_2 lamp taken with the iKon-M camera. The visible edge in the row 640 likely stems from artifacts of the focusing mirror. The region with the lowest width of the 121.5 nm peak, marked on the image with red lines, is used for generation of the spectrum.

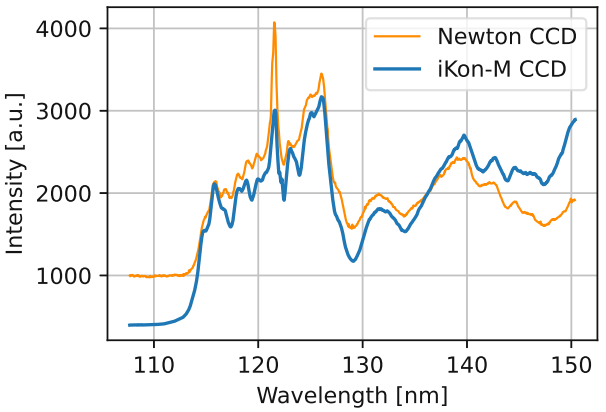

Figure 15: Spectrum of a D_2 lamp as seen by a iKon camera, calculated from pixel data shown in figure 14. Calibration data was taken from (9). For comparison, a part of the spectrum of the same lamp taken with the Newton camera, shown in full in figure 16b is shown.

Die approbierte gedruckte Originalversion dieser Diplomarbeit ist an der TU Wien Bibliothek verfügbar
The approved original version of this thesis is available in print at TU Wien Bibliothek.

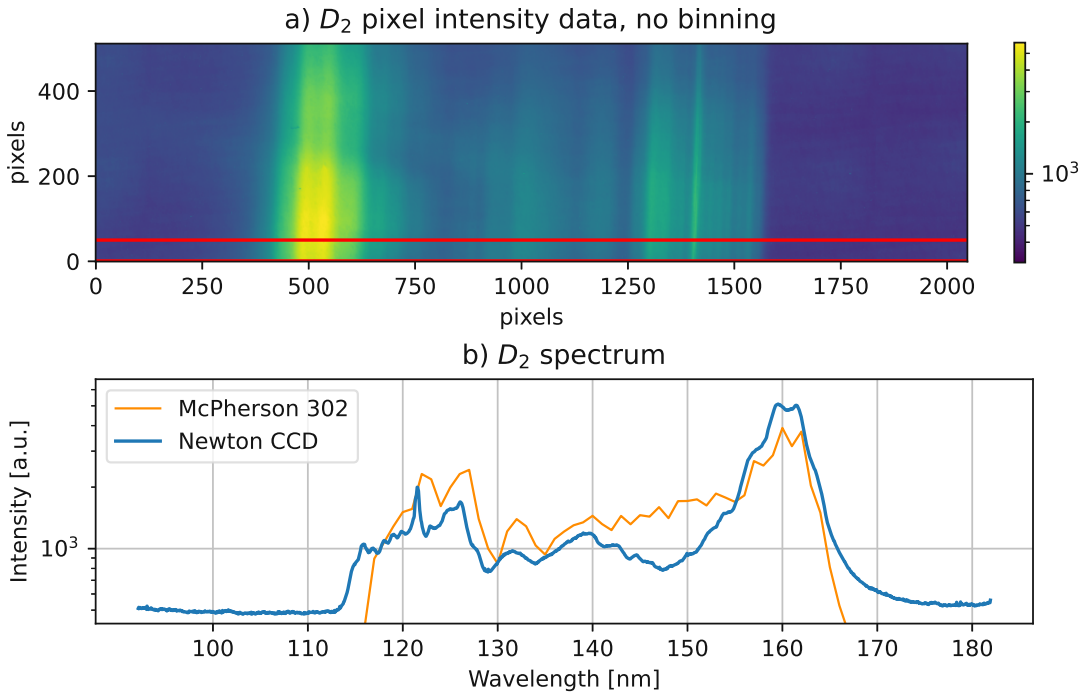

Figure 16: Logarithmic plots of raw pixel data (a) and calculated spectrum (b) of a D_2 lamp as seen by the Newton camera. The characteristic spectrum was calculated using the first 50 rows, denoted with red bars in (a), and calibration data from listing (10). The camera was not cooled during measurement, leading to the comparatively high noise floor. The spectrum is flipped compared to the image. For comparison, a spectrum of a D_2 lamp taken with a McPherson 302 monochromator further discussed in section 6 is shown.

spectrum. The raw pixel data with markings of the used area are shown in figure 16a. Neither cooling nor binning were used. Exposure time was set to 10 s, shift speed and readout rate to 57.71 µs and 3 MHz, respectively.

The calculated spectrum nicely aligns with the one taken with the iKon-M camera, as can be seen in figure 15. The two peaks around 160 nm are resolved as well and within 0.5 nm of the peaks as seen by the McPherson 302 monochromator. A significant noise floor remains due to the lack of cooling, binning and any other noise reduction techniques.

3.4 Noise characterization

As described in section 2.3.2, noise on the CCD can in general be separated into read noise and dark current. Read noise can be characterized as the standard deviation of a entirely dark shot of zero exposure time.

For our calculation, a measurement with an exposure time of 10 µs, 4x4 binning, 57.71 µs vertical shift speed and a 0.05 MHz pixel readout rate at −60 °C was made. Two frames were taken and gave a standard deviation of 1.18. Frames had an average baseline value of 549. This measurement cannot account for fixed pattern noise as we did not have access to a uniformly illuminating light source.

To estimate dark current, a measurement of with the same parameters as the bias frame but with 1800 s exposure time was performed with 28 frames taken. For each, the average baseline of the bias frame was subtracted. Outliers higher than 4000, representing the highest 0.0008% of values, were removed as they likely were caused by cosmic rays. The result was a mean dark count rate of 0.0082 per second

Die approbierte gedruckte Originalversion dieser Diplomarbeit ist an der TU Wien Bibliothek verfügbar
The approved original version of this thesis is available in print at TU Wien Bibliothek.
TU Bibliothek Your knowledge hub WIEN

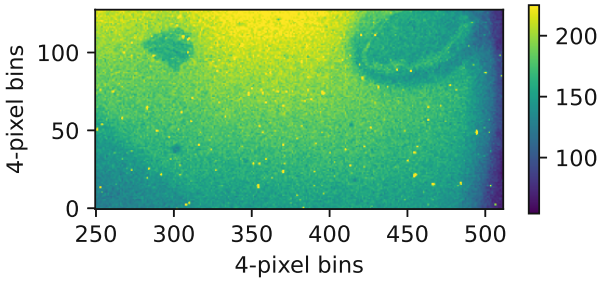

Figure 17: Residual substances seen on the Newton CCD after cooling to −61 °C and integrating without external signal for 1800 s. 4x4 binning was applied, vertical shift speed was 57.71 µs and pixel readout rate was 0.05 MHz.

which is too close to the read noise to be considered significant. This aligns well with literature, stating that dark current reaches the order of the read noise when cooled [26].

Another factor that needs considering when cooling the CCD sensor is residual water vapor and similar substances freezing and sticking into the chip. Such artifacts produce variations on the image that are usually easily recognized and leave little to no trace when the chip heats up again. An exemplary frame taken with residuals from cooling is shown in figure 17, where two artifacts can be identified in the rows around the index 100: one smaller around column index 300, the other around column index 450.

4 Spectrometer with MCP detector

Now that we have successfully characterized the spectrometer using different CCD cameras and established precise calibrations for them, we are ready for the "next level": the MCP detector.

The spectrometer with the MCP detector uses the same spectral apparatus and slit mentioned in section 3. Instead of an angle adapter and CCD camera, an MCP chamber is attached to the grating chamber. Inside the MCP chamber, a Hamamatsu F3490-21P-Y006 micro channel plate (MCP) with serial number 20101201 is mounted under an 32° angle [16]. The MCP consists of two amplification stages with 12 µm channel diameter under a bias angle of 8°. The length-diameter ratio of the channels is 40. A P46(ITO) phosphor screen to convert electrons into visible light is mounted on the rear end [20]. The P46 phosphor screen consists of Ce^{3+}:$Y_3Al_5O_{12}$ crystal grains, emitting at a peak wavelength of 530 nm with a 10% decay time of 150 ns [38].The front end of the MCP is coated with CsI and therefore solar-blind. Behind the MCP, a rectangular mirror supplied by EKSMA Optics is mounted.

The light emitted by the phosphor screen is redirected through a vacuum viewport towards a QHYCCD QHY290 monochrome camera, serial numbers 100084 and 037353, with an Edmunds Optics #59-872 lens [10]. The camera comes with a Sony IMX290 CMOS chip with a pixel array of 1920×1080 square pixels with a size of 2.9 µm each. The full well capacity is larger than 15 000 e^- and the ADC has a bit depth of 12 bits. Readout noise is specified to be 0.75 e^- for high gain and 3.2 e^- for low gain settings.

A black coated aluminum tube is used to shield against ambient light. A schematic of the setup including the most important components is given in figure 18.

Power is applied to the MCP by an iseg THQ 2CH 60W power supply, model number T207006, preconfigured to operate channel 1 in negative voltage configuration up to −2 kV and channel 2 in negative voltage configuration up to 4 kV. Channel 1 is connected to the "MCP In" pin, providing the acceleration voltage for electrons in the first amplification stage. Channel 2 is connected to the "P" pin, providing positive acceleration voltage for the second amplification stage onto the phosphor screen.

The third connector, "MCP Out", is connected to ground using a hand-made 10 kV-SHV connector that connects signal and shield-

Die approbierte gedruckte Originalversion dieser Diplomarbeit ist an der TU Wien Bibliothek verfügbar
The approved original version of this thesis is available in print at TU Wien Bibliothek.
TU Bibliothek Your knowledge hub WIEN

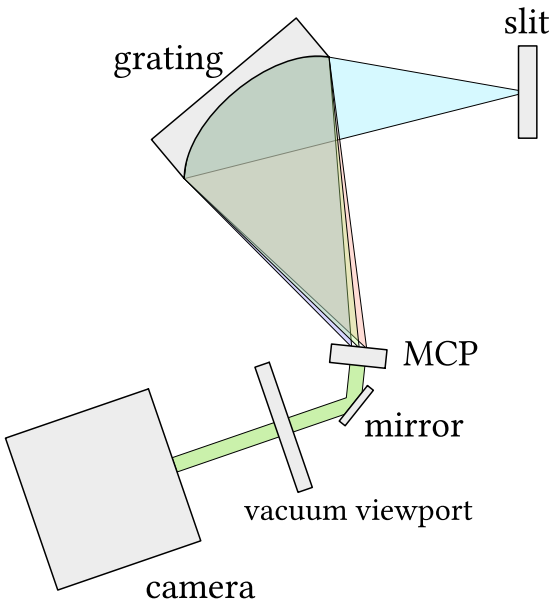

Figure 18: Schematic drawing of the spectrometer with the MCP module mounted. The light of a probe or light source enters through the slit and falls onto the grating. Different wavelengths are focused simultaneously on the MCP on different positions. On the MCP, photons are converted to electrons which are then amplified and accelerated until they hit the phosphor screen on the back side of the MCP. Visible, green light is produced and reflected onto the camera outside of the vacuum system.

ing. For that part, a Winchester Electronics Kings type 1065-1 QD connector was used. The shielding of the feedthrough is connected to the shielding of all the cables and to ground through the high-voltage supply.

4.1 Vacuum preparation

The vacuum of the system proved unsuitable for installation of the MCP at first. According to the supplied manual, the MCP should be held constantly under pressures below $1.3{\cdot}10^{-6}$ mbar [15] but the chamber could only be pumped to $3 \cdot 10^{-3}$ mbar. According to the manufacturer H+P spectroscopy, the chamber should be able to provide a vacuum of $1 \cdot 10^{-6}$ mbar [15], being limited only be the ISO flanges used. Due to shortcomings of their supplier, the entire vessel is coated in highly absorbing paint, unfortunately including the area at the flanges. Various tests indicated that the coating in these key areas around the flanges is leaky and responsible for the bad vacuum.

First, a helium leak detector was connected to the system. It works by continuously scanning the gas pumped out of the system using a mass spectrometer tuned to ^{4}He. Then, ^{4}He gas is sprayed in small quantities close to suspected leaks. The longer it takes for the mass spectrometer to report rising levels, the further away and smaller the leak is. Using this method, essentially all the joints between the grating chamber, the slit channel and the detector module could be identified as leaking. All these joints are painted.

Visual inspection of the coating surface around the joints showed multiple small scratches. Spraying the area with sealing paint and letting it dry created a smooth surface and improved the leak rates of the joint. This is another indication that scratches in the paint were responsible for the leaky joints.

Coated joints were finally covered with a thin layer of vacuum grease by which they became practically He tight. Presumably the grease filled the small scratches on the coating surface. After this treatment pressures of $3.0{\cdot}10^{-6}$ mbar could be reached.

Even after this treatment, the time needed to pump below $1 \cdot 10^{-5}$ mbar remained in the order of hours. If, however, the system was only opened for a very short time in the order of a minute or less, a good vacuum was achievable shortly after again. The reason for this was not evaluated precisely but multiple effects could play a role here.

Firstly, the lab in which the apparatus is situated tends to have high air humidity and therefore, more water in the air. Hence, more water might get stuck on the inner walls when opening the setup, leading to longer pumping

Die approbierte gedruckte Originalversion dieser Diplomarbeit ist an der TU Wien Bibliothek verfügbar
The approved original version of this thesis is available in print at TU Wien Bibliothek.

times.

Secondly, the vacuum grease in the system might be the subject of outgassing, thereby further reducing the achievable pressure.

Wether outgassing or water vapor play a role here could be further evaluated using a mass spectrometer.

Even after all possible optimizations to the vacuum vessel, the optimal operating pressures for the MCP of below $1.3 \cdot 10^{-6}$ mbar could not be reached. The conditions we are able to reach are however sufficiently close so that we can operate the MCP, albeit possibly under suboptimal noise characteristics.

4.2 Analysis and interpretation of MCP signal

Once the MCP is supplied with a high enough voltage, green dots appear on the phosphor screen. A picture of these dots is given in figure 19. These are then imaged using a fixed monochrome camera and the images are transferred to a computer where the processing is done. As the MCP is used as a detector for single photons, resolving single dots on the phosphor screen is crucial and a dot detection and fitting algorithm must be employed.

Dots vary greatly in size and intensity depending on the supplied voltages, and vary greatly in number depending on the amount of photons hitting the detector, as detailed in section 4.3. So the precise position of each dot is the most relevant information for our use case. Ideally, the detection scheme should allow to collect as many dots as possible, precisely fitting the central position of each one. That means that we want to make exposure times on the camera short enough so that dots on the pictures do not overlap. Figure 20b shows a case in which dots overlap and cannot be distinguished anymore.

However, we cannot reduce exposure times indefinitely. The shorter we expose, the larger becomes the total fraction of time spent for readout. And the more time we spend on readout, the more likely it is for a dot to appear

Figure 19: Real-color photo of the MCP signal of a vacuum gauge as seen through the viewport, taken with a smartphone camera. The left strip visible on the image is the actual MCP whereas the right strip is the image reflected by the mirror.

just during that time. Due to the nature of the rolling shutter employed in the camera this leads to images with half-dots or only halos of dots on them as shown in Figure 20c. These make analysis more difficult and should therefore be avoided.

Once a reasonable exposure time is found, one can then start with image analysis. Various steps need to be performed to come from the raw image to usable spectral data:

- Extract dots from images
- For each dot, calculate its central position
- Convert central positions of dots to spectral information

Maybe most importantly, each of these steps needs to be performed in a reliable, verifiable way in order to build trust that measurements done with the setup indeed are correct.

Die approbierte gedruckte Originalversion dieser Diplomarbeit ist an der TU Wien Bibliothek verfügbar
The approved original version of this thesis is available in print at TU Wien Bibliothek.
TU Bibliothek Your knowledge hub WIEN

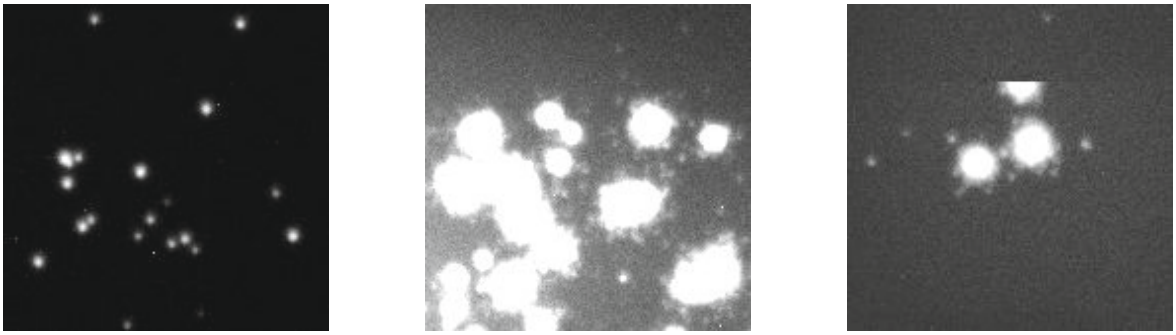

(a) Individual dots (b) Overlapping dots (c) Half-dot

Figure 20: Different possible images of dots on the MCP as seen by the camera. Intensities of images 20a & 20c have been scaled for better visibility. Images 20b & 20c were taken at maximum MCP supply voltage whereas image 20a was taken with MCP In = 1.375 kV and P = 3.5 kV.

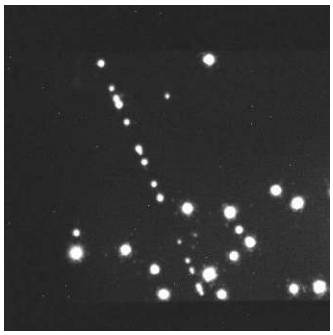

Figure 21: Trace of likely a high-energy particle traversing the MCP detector. The MCP was operated with $U_{\mathrm{MCPin}} = 2\,\mathrm{kV}$ and $U_{\mathrm{P}} = 3\,\mathrm{kV}$.

4.2.1 Sources of noise

To get the best possible results, it is advisable to be aware of the different sources of noise in the system. Each type of noise originates from a different phenomenon and has different influences on the system.

dark noise on the MCP detector

As PMTs, MCPs as well have a very low dark count rate. The dark count rate was found to increase with increasing supply voltages, detailed later in section 4.3.2. This seems to be in contrast with measurements from literature which have found no dependence of dark noise to voltage on an MCP alone [12] and are detailed in section 2.4.1. Direct comparison was unfortunately not possible since our setup uses an additional phosphor screen not present in [12].

It is desirable to keep dark noise on the MCP detector as low as possible. Dark noise has a constant term, but can have a time dependent component as well, usually due to outgassing. Bake-out or operating for some hours under vacuum can help reduce this term to a minimum. Assuming vacuum pressure stays constant, the time dependent term should only be decreasing over time.

cosmic particles on the MCP detector

Cosmic particles traverse practically all matter on earth. On PMTs, a cosmic particle leads to a characteristic burst of many counts that can easily be filtered out. On MCPs however this is nontrivial, as cosmic particles create dots with comparable intensity and size to signal. Their trace is however characteristic. A probably cosmic particle trace is shown in figure 21. Removal of such cosmic particle traces is non-trivial. However, such events rarely happen and have only a negligible impact on measurements [12].

Die approbierte gedruckte Originalversion dieser Diplomarbeit ist an der TU Wien Bibliothek verfügbar
The approved original version of this thesis is available in print at TU Wien Bibliothek.
TU Bibliothek Your knowledge hub WIEN

noise on the CMOS camera

Both thermal noise and readout noise have an impact on the images produced by the camera. Thermal noise can lead to "hot pixels" with much higher values than their surroundings, if amplified by manufacturing defects. These lead to typical "salt and pepper" noise which can be removed either by neglecting any potential dots smaller than a few pixels or by applying a median filter. Readout noise does not produce high values on pixels and is therefore also not a problem.

stray light in the system

The MCP is coated with CsI so it is solar-blind and unaffected by stray light. The camera however is very sensitive to it, even with the supplied light shield installed. Depending on the detection algorithm, stray light reflecting from the casing of the MCP can lead to high false positive rates and low precision. It can be avoided easily by wrapping the relevant part with aluminum foil and/or turning off the light.

4.2.2 Extraction of dots from images

In a first step, hot pixels from the CMOS camera need to be removed. Such pixels do not change between frames and usually have comparatively very high pixel values. As images are mostly dark, these pixels have much higher values than their surrounding. Comparing each pixel with its neighbors and flagging those that are both much higher than the average of their surrounding and much closer to the image maximum than the image median proved successful. Hot pixels can reliably be removed by this technique without requiring multiple images.

A different method for the first step could have been to compare multiple images of the same measurement and flag pixels that have both comparatively high values and the same values between frames.

The second step then involves finding pixels that are considered to be signal. Different approaches using different statistical quantities were attempted here, with varying degrees of success.

Feature detection algorithms are often characterized by their precision and recall. Precision in this context refers to the share of selected dots that are actually dots. Recall on the other hand is defined as the ratio of found dots to the total number of dots. A good algorithm will detect all dots (high recall) but nothing else (high precision).

This extraction is possible with good accuracy and low complexity as no features other than dots are visible on the images.

mean and standard deviation:

Marking pixels as signal that are higher than a certain factor times the image standard deviation added to the mean is not suitable as a measure of signal. This is because both standard deviation and mean are heavily influenced by outliers, like in this case signal dots. Depending on the amount of dots on the image the threshold for detection would shift which is unacceptable in this case.

median and inter-quartile range:

The inter-quartile range (IQR) is defined as the difference between the 75% and 25% quantiles of the data. It is then multiplied by a chosen factor and added to the median to get a threshold. All pixels with higher values than the threshold are then considered signal candidates.

As the median and the IQR generally increase with noise, this algorithm is in principle robust and gives good results. In situations where the intensity of the dots is low, e.g. because of very low gain settings or low voltages supplied to the MCP, dots are not detected reliably anymore. The reverse is also possible, so that in low noise situations the IQR gets too small or even 0, in which case much of the noise is wrongly identified as dots.

Die approbierte gedruckte Originalversion dieser Diplomarbeit ist an der TU Wien Bibliothek verfügbar
The approved original version of this thesis is available in print at TU Wien Bibliothek.
TU Bibliothek Your knowledge hub WIEN

maximum-dependent threshold:

The uncooled CMOS sensor always introduces hot pixels, the values of which depend mainly on the camera gain. The maximum value will therefore always be much higher than the actual background values. Marking pixels as signal that are higher than a specified fraction of this maximum value therefore reliably selects dots if the signal to noise ratio in the image is good enough. A proper threshold value needs to be found by the user for each combination of camera gain and MCP supply voltage.

While simple and usually robust, a very efficient hot pixel removal stage or cooling of the camera might lower the maximum of images without dots, potentially leading to greatly reduced precision.

Gaussian filtering:

Another approach to dot detection performs median filtering first, and in a second step, applies a Gaussian filter.

For this approach to give reasonable results, the correct width σ of the Gaussian is key. A too large width will smooth out the dots as well, whereas a too small width will leave noise. The width of the Gaussian is therefore first approximated from a representative dataset. For that, a 1D Gaussian distribution is fitted both vertically and horizontally into the maximum of each image and the average of the fitted widths is stored. Widths too large or too small to be reasonable are excluded from the dataset. Finally, the median of the calculated values serves as estimation of σ, and hence the expected dot size.

After each filtering step, a threshold is also applied. In the final step, dot candidates too large to be real dots are sorted out. Only dots with areas two standard deviations below the mean or smaller are kept.

This approach is robust when the correct σ is chosen. However, calculation of the correct σ is not straightforward and the optimal σ depends on the voltages supplied to the MCP and phosphor screen. It is the most complex of the algorithms studies while not providing significant benefits.

Any statistical quantities used in the determination of signal pixels need to be checked against evaluating to zero and precautions for these cases need to be made.

In the next step, adjacent pixels are grouped together to dots and given an index. Standard routines from the scipy library [46] are used for this step.

Some noise, for example adjacent hot pixels, usually passes through the hot pixel removal, resulting in small artifacts also seen as dots by the algorithm. These are filtered by deleting dots smaller than 4 pixels. This filtering works reliably as real dots are usually much larger.

The actual algorithm used in the processing of images is specified for each measurement. Mostly, the maximum-dependent threshold algorithm was used as it is straightforward to understand and implement and was found to give reasonable results.

4.2.3 Calculation of each dot's central position

One possible approach to detect the center point of a dot would be to fit a 2D Gaussian distribution with variable position. This however requires considerable calculation resources.

A simpler approach was chosen instead, calculating the center of each dot as a mean of the positions of each assigned pixel, weighted by their intensity. This approach gave satisfactory results while being fast.

4.2.4 Conversion of pixel value to wavelength

As the geometrical setup allowed us to do so, simply the vertical axis of the image was chosen as starting point for wavelength calculation

Die approbierte gedruckte Originalversion dieser Diplomarbeit ist an der TU Wien Bibliothek verfügbar
The approved original version of this thesis is available in print at TU Wien Bibliothek.
TU Bibliothek Your knowledge hub WIEN

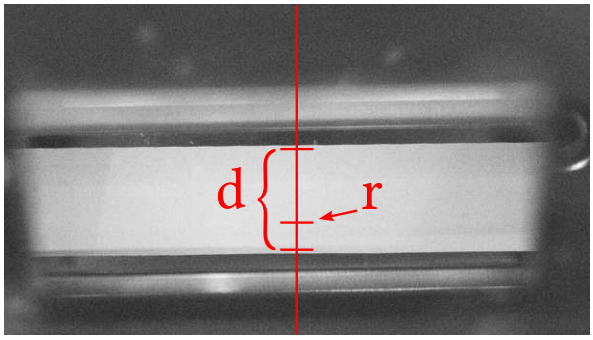

Figure 22: Image of the camera as it sees the MCP via the mirror. The distance $d = 19.7\,\text{nm}$ marks the usable wavelength range covered by the MCP. The position $r = 710.9\,\text{px}$ marks where the wavelength shown by the grating controller software is imaged. The start and the end of the MCP are at 469.1 px and 799.2 px. Pixel values are counted from the top.

during the characterization. The camera rotation and view on the MCP might change in the future, in which case the conversion also needs to be adapted accordingly.

For the calibration, three images at three different wavelengths covering the entire width of the MCP were taken. Pixel values of the peaks were extracted and matched with the wavelength set on the grating rotation stage. The positions and values measured are displayed in figure 22.

The upper bound was found to be at $r_\text{u} = 469.1\,\text{px}$, the lower bound at $r_\text{l} = 799.2\,\text{px}$. The spectral distance covered between them was $d = 19.7\,\text{nm}$. Pixel coordinates are always measured from the top of the image. Using

$$a_\text{nm,px} = \frac{d}{r_\text{l} - r_\text{u}}, \tag{11}$$

the conversion factor between pixel and wavelength in nanometer can be calculated.

The wavelength reference r describes where on the camera image the wavelength given by the grating controller software appears. Finally, knowing the position of the grating expressed as wavelength p, the vertical positions of the dots x can be converted to wavelengths y via

$$y = p + (x - r) \cdot a_\text{nm,px}. \tag{12}$$

For the specific camera position used during this work, the required values for this conversion were calculated to be

$$\begin{aligned} a_\text{nm,px} &= 0.0597\,\text{nm/px}, \\ r &= 710.9\,\text{px} \end{aligned} \tag{13}$$

With the camera positioned in this way, the detector chain is already suitable for resolving sub-nanometer and even sub-ångstrom features in the spectrum. In theory, the conversion factor $a_\text{nm,px}$ can be further optimized by rotating the camera by 90° and reducing the distance towards the mirror so that the shorter side of the MCP covers the entire longer side of the camera view. While this is recommended by the manufacturer, it has not been performed during the course of this work as the wide field-of-view proved useful for debugging and the spectral resolution has likely been limited by different factors than camera resolution.

4.2.5 Quality control

The quality of the algorithms described was tested by overlaying detected dots on the original image and visually comparing the results. It was checked that the detected dots matched the actual dot pixels as well as that no or a very small number of dots were missed by the algorithm. Selection of images to check was done by random sampling but by investigating suspicious results as well. No quantitative results were collected.

4.2.6 Data storage

The camera in principle supports an image bit depth of 16 bit. By default, data are therefore stored losslessly compressed as PNG images, resulting in file sizes of 2.1 MB on average when a gain of 330 is used. When taking many images this quickly requires massive amounts of storage. Considerable size reductions are easily possible using well-established methods like

Die approbierte gedruckte Originalversion dieser Diplomarbeit ist an der TU Wien Bibliothek verfügbar
The approved original version of this thesis is available in print at TU Wien Bibliothek.
TU Bibliothek Your knowledge hub WIEN

storing with only 8 bit depth or even lossy conversion using JPEG (Joint Photographic Expert Group) compression.

These methods have been investigated and compared to lossless data taking. Simply reducing bit depth to 8 bit leads to an average image size of 0.68 MB, a reduction to 32%. Saving images as JPEG with a quality factor of 75% even leads to an average image size of 0.01 MB. The effect on dot detection highly depends on the signal to noise ratio of the dots on the images. If chosen carefully, there is no impact at all in terms of detected number of dots and under 1% change in detected dot size. This is in general true for storing 8 bit PNGs (Portable Network Graphics) instead of 16 bit when using the threshold algorithm in environments were the threshold can be set to 0.6 or higher. Exemplary conditions can be taken from table 1.

Storing data with reduced precision and lossy compression techniques can be accomplished if suitable operating parameters for MCP and camera are selected. However, considerate testing should be done before using it in a production environment.

4.3 Optimization of measurement parameters

The planned use of the spectrometer involves a possibly very weak signal at a very specific but imprecisely known wavelength that will lose intensity over hours, if not minutes. Therefore, the following characteristics of the spectrometer should be optimized:

- Signal rate
- Signal to Noise ratio (SNR)
- Spectral resolution

The detector chain consists of two parts, MCP and camera. Each of those has its own set of parameters that can be modified within a certain range:

- MCP In to MCP Out voltage, between 0 and 2000 V
- MCP Out to P voltage, between 0 and 4000 V
- Camera gain, between 0 and 729 (arbitrary units)
- Camera exposure time, between 10 ms and effectively 3600 s.
- Camera cooler

In section 4.2, limitations for too low or too high exposure times were already presented. A trade-off needs to be made. The exposure time has to be short enough to minimize the probability of overlapping dots but long enough to minimize the possibility of missing generating half-dots and other readout artifacts. Typically useful values range from 0.1 s to 5 s, depending on both the amount of signal hitting the MCP detector and the voltage supplied to it.

4.3.1 MCP voltage characterization setup

The effects of different voltages on the MCP are less trivial to analyze. Therefore, over the course of this work data for various different voltages between the “MCP In” and “MCP Out” pin, U_{MCPin}, and between the “MCP Out” and “P” pin, U_{P}, were collected, with and without a VUV light source attached.

Voltages below $U_{\mathrm{MCPin}} < 1200\,\mathrm{V}$ or $U_{\mathrm{P}} < 1000\,\mathrm{V}$ did not produce sufficiently intense dots anymore and detection became unreliable. Cooling the camera might help at detecting dots with even lower intensities, as might increasing the gain settings and adapting the dot detection algorithm accordingly. This was however not done.

Voltages higher than these were scanned in steps of 200 V and 500 V, respectively, starting with the highest voltage. For each U_{MCPin}, the entire range of U_{P} was scanned, and only then U_{MCPin} was modified. The exposure time was adjusted to be able to still resolve dots at full high voltage (HV), resulting in 0.1 s per frame

Die approbierte gedruckte Originalversion dieser Diplomarbeit ist an der TU Wien Bibliothek verfügbar
The approved original version of this thesis is available in print at TU Wien Bibliothek.
TU Bibliothek Your knowledge hub WIEN

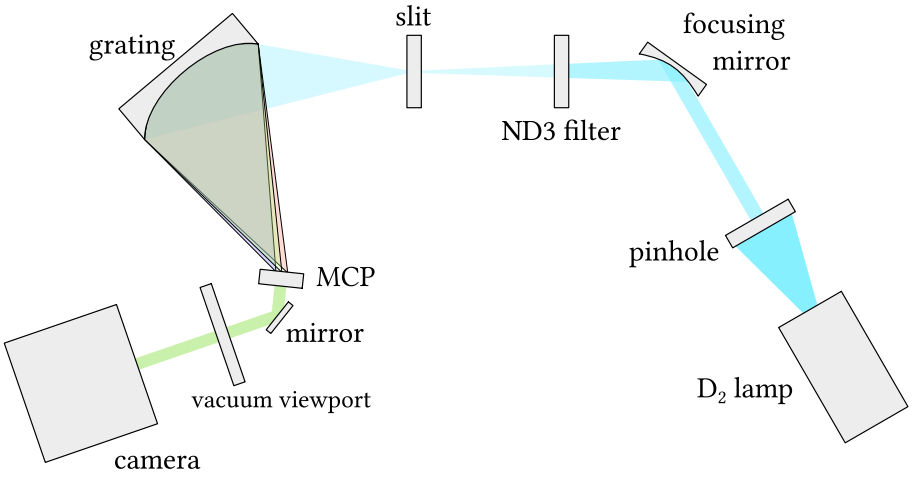

Figure 23: Schematic view of a low-intensity D_2 light source for MCP characterization measurements, connected to the system. The pinhole has a diameter of 150 µm and the slit is smaller than 300 µm.

for the signal measurement and 1.0 s per frame for the dark measurement.

For each combination of voltages, 60 frames were taken. The camera gain was set to 330, and no cooling was used. Every 10 distinct combinations of voltages, the initial configuration was remeasured to ensure that no drift in the signal intensity occurred.

To generate sufficiently low signal, a D_2 lamp was attached behind a 150 µm pinhole, then focused onto the slit using a mirror. Between mirror and slit, a ND3 filter was attached, damping signal by three orders of magnitude. The slit was opened no wider than 300 µm. The grating was adjusted to image the 160 nm region onto the MCP, so that the MCP gets illuminated broadly. A schematic visualization of the setup is given in figure 23.

For processing of the images, a suitable threshold, that is, a suitable percentage of the maximum value of each image later used for dot detection, was first established. This was done manually for each combination of voltages, favoring optimal precision over recall and led to the threshold table, table 1. This threshold table already shows that lower voltages led to less intense dots that are harder to detect.

Each image was then searched for dots using the threshold algorithm detailed in section

U_P [V]	U_{MCPin} [V]				
	2000	1800	1600	1400	1200
4000	0.9	0.6	0.6	0.6	0.2
3500	0.9	0.6	0.6	0.2	0.2
3000	0.9	0.6	0.6	0.2	0.2
2500	0.9	0.6	0.4	0.2	0.12
2000	0.9	0.5	0.2	0.2	0.12
1500	0.6	0.3	0.2	0.15	
1000	0.2	0.2	0.2	0.15	

Table 1: Relative thresholds used for dot detection at different voltage combinations. Thresholds were selected manually, optimizing on precision rather than recall. At $U_{MCPin} = 1200$, $U_P \leq 1500$, reliable results were not possible anymore using the selected algorithm, so no value is given.

Die approbierte gedruckte Originalversion dieser Diplomarbeit ist an der TU Wien Bibliothek verfügbar
The approved original version of this thesis is available in print at TU Wien Bibliothek.

4.2.2, with the threshold set to the fraction of the maximum value specified in table 1. The resulting coordinates, sizes and intensities of dots were stored in accompanying CSV (comma-separated values) files for further analysis.

4.3.2 MCP voltage characterization results

From the collected data, a variety of observations can be made.

Firstly, the MCP efficiency shows no trivial time dependence over the course of the experiment. Both dark and signal rates stayed within their expected variations. Dark count rates for $U_{\mathrm{MCPin}} = 2000\,\mathrm{V}$ and $U_{\mathrm{P}} = 4000\,\mathrm{V}$ lie between $1.0\,\mathrm{s}^{-1}$ and $1.3\,\mathrm{s}^{-1}$ over a timeframe of 2.5 h, thereby staying well within one standard deviation. Signal count rates for the same voltage and timeframe varied between $43\,\mathrm{s}^{-1}$ and $76\,\mathrm{s}^{-1}$, exceeding one standard deviation. This does not come entirely unexpected as the D_2 lamp is known to slightly drift in intensity [2, 37]. The data further contains one anomaly. In the first half hour of the signal run, the number of dots gradually decreased much more than expected by the decreasing voltages. Then, 29 minutes and 40 seconds into the experiment, dot count rates suddenly increased by a factor of almost 7. The effect is shown in figure 24. This means that all previous measurements are likely tainted. Affected are all measurements with $U_{\mathrm{MCPin}} = 2\,\mathrm{kV}$ except the full HV measurement, $U_{\mathrm{MCPin}} = 2\,\mathrm{kV}$, $U_{\mathrm{P}} = 4\,\mathrm{kV}$ which has been repeated multiple times to study time dependence. Also affected are the measurements for $U_{\mathrm{P}} = 4\,\mathrm{kV}, 3.5\,\mathrm{kV}$ at $U_{\mathrm{MCPin}} = 1.8\,\mathrm{kV}$. One possible reason for this effect could be instabilities in the arc of the D_2 lamp.

Secondly, dark count rates are lower than stated in the test sheet supplied with the MCP. In it, a dark count rate of $1.31\,\mathrm{s}^{-1}\mathrm{cm}^{-1}$ was specified for full HV. In this experiment, an area of $3\,\mathrm{cm}^2$, or 69% of the entire MCP, was imaged on the camera, leading us to expect a dark count rate of $3.99\,\mathrm{s}^{-1}$. Instead, we found the real dark count rate to be only $1.19\,\mathrm{s}^{-1}$, or

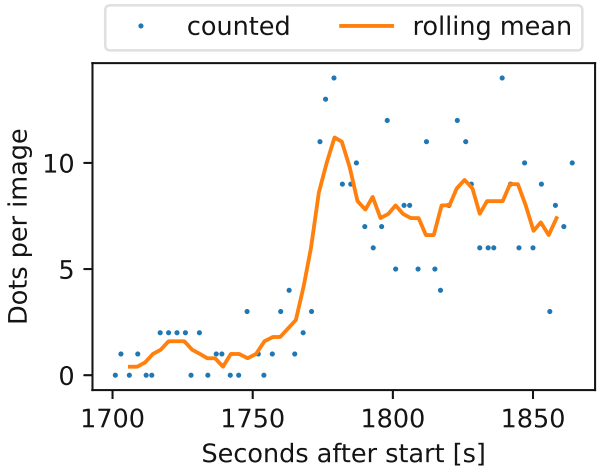

Figure 24: Counted dots and 5-point rolling average for the second measurement of $U_{\mathrm{MCPin}} = 2\,\mathrm{kV}$ and $U_{\mathrm{P}} = 4\,\mathrm{kV}$. The abscissa shows seconds after start of the experiment. Exposure time was 0.1 s and gain 330. At 1775 s after start, a rise of dot counts per image of a factor of 7 appears.

when calculated per area, $0.39\,\mathrm{s}^{-1}\mathrm{cm}^{-1}$.

Dark noise behaves similarly to what one might intuitively think. Lower voltages approximately lead to lower count rates. This is less true for signal count rates which are considerably different for different combinations of voltages. Because of this, different voltage combinations also give different signal to noise ratios (SNR). Dark count rates, signal count rates and the resulting SNR for the measured voltages are shown in figure 26.

Dark count rates have a clear maximum at full HV and become very low for low "MCP In" voltages. Signal count rates on the other hand are not particularly high at full HV even when excluding possibly tainted results. When combined, this leads to three interesting regions with high SNR, ordered by U_{MCPin}:

1. $U_{\mathrm{MCPin}} = 1.8\,\mathrm{kV}, U_{\mathrm{P}} = 1\,\mathrm{kV}$,
2. $U_{\mathrm{MCPin}} = 1.6\,\mathrm{kV}, U_{\mathrm{P}} = 2.5\,\mathrm{kV}$,
3. $U_{\mathrm{MCPin}} = 1.4\,\mathrm{kV}, U_{\mathrm{P}} = 3.5\,\mathrm{kV}$.

Die approbierte gedruckte Originalversion dieser Diplomarbeit ist an der TU Wien Bibliothek verfügbar
The approved original version of this thesis is available in print at TU Wien Bibliothek.
TU Bibliothek Your knowledge hub WIEN

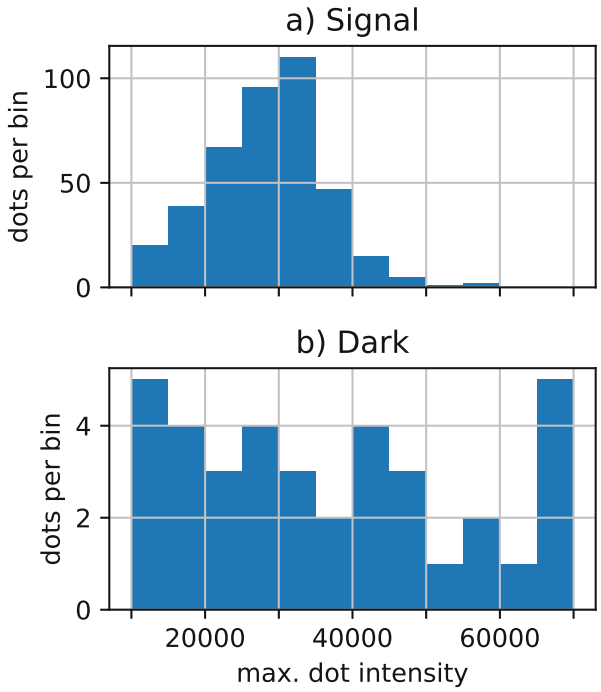

Figure 25: Histograms of signal and dark dot intensities, measured at $U_{\mathrm{MCPin}} = 1.6\,\mathrm{kV}$ and $U_{\mathrm{P}} = 1.5\,\mathrm{kV}$. Of 37 counts in the dark measurement, around 14% saturated the pixel whereas this did not occur even for one of the 402 dots in the signal measurement.

These regions are characterized by good signal rates while at the same time having particularly low noise rates, hence both signal rate and signal to noise ratio are optimal there.

In terms of brightness of the dots some comparisons can be made and preliminary data indicates that dots emerging from dark counts might have a tendency to be more intense. In the experiments performed so far, only data below a certain voltage level can be meaningfully analyzed since dots of higher voltages immediately saturated the affected pixels. Comparing the maximum pixel value of dots from signal and dark measurements at $U_{\mathrm{MCPin}} = 1.6\,\mathrm{kV}$ and $U_{\mathrm{P}} = 1.5\,\mathrm{kV}$, a shift of the distribution is clearly visible. Histograms of the maximum dot values are presented in figure 25. While dots of the signal measurement have a mean maximum intensity of approximately $2.8 \cdot 10^4$, dots of the dark measurement reach a value of around $3.7 \cdot 10^4$. The histograms show that dark dots more often reach maximum intensity, possibly stemming from high-energy electrons being released or generated inside the MCP. Signal dots were less intense. As not even one dot of the signal set saturated camera pixels it might be possible that such a signal prevents high-intensity dark counts from happening. However, statistics on these results are poor and not yet reliable to draw conclusions.

A histogram of dot brightnesses should correspond to some extent to a pulse height distribution (PHD) that a multichannel analyzer would produce. This depends however on the linearity of the phosphor layer in terms of photon yield per impinging electron and per acceleration energy, as well as the linearity of the CMOS sensor itself. If a PHD is desired alongside spatial information, calibration with a multichannel analyzer could be done in parallel to find a relation between pixel value at given camera settings and pulse height.

The three supply voltage regions with particularly high SNR can also be compared in terms of compression potential. Region 1 dot counts deviate 0.2% when stored as 8 bit PNG and 1.6% when stored as 75%-quality JPEG. Region 2 only deviates when stored as JPEG while dot count rates in region 3 stayed precisely the same for both tested compression option. Only region 3 is therefore suitable for compressed data storage. Dot sizes deviated in all cases by less than 2%, with region 3 being most affected. As dot sizes do not reflect any physical quantity of interest, this does not hinder the regions fitness for compressed storage.

While these results were generated with the utmost care, different dot counting methods may have higher (or lower) precision and recall and therefore slightly different count rates.

To come to a well-optimized setup, MCP voltages, camera settings and dot detection algorithm need to be closely integrated. This can be done by selecting a combination of MCP supply voltages with high signal rate and high

Die approbierte gedruckte Originalversion dieser Diplomarbeit ist an der TU Wien Bibliothek verfügbar
The approved original version of this thesis is available in print at TU Wien Bibliothek.
TU Bibliothek Your knowledge hub WIEN

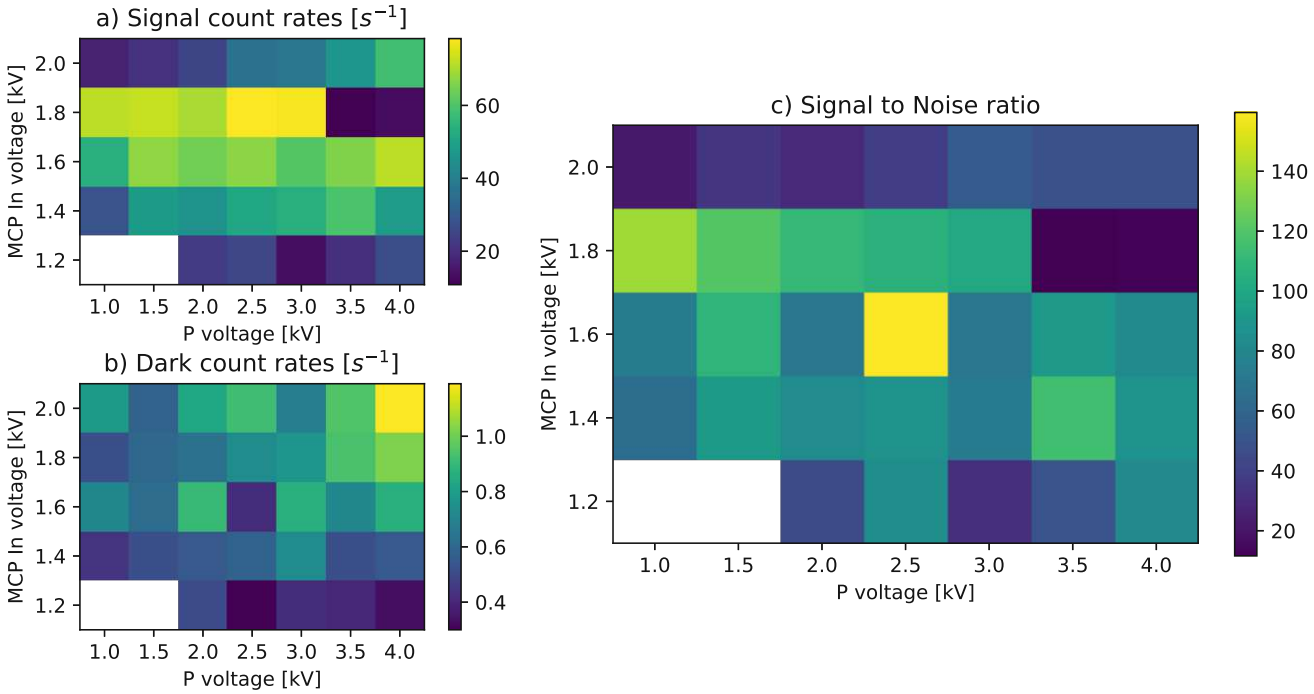

Figure 26: Signal (a) and dark (b) count rates for different combinations of MCP supply voltages, as well as signal to noise ratios (SNR)(c). The exposure time for the signal run was 0.1 s so measured values are multiplied by 10 to be comparable. The exposure time of dark run was 1.0 s, so no scaling was applied. White quadrants did not provide valid results, i.e. dots could not be reliably identified anymore.

SNR first and adjusting camera settings and dot detection algorithm afterwards for maximum precision and recall.

4.4 Measurement of a D_2 lamp spectrum

As described above and shown in figure 23, a D_2 lamp was installed in such a way that only very little light hits the MCP. For this lamp, a spectrum around 160 nm was measured using supply voltages of $U_{\mathrm{MCPin}} = 1.375\,\mathrm{kV}$ and $U_{\mathrm{P}} = 3.5\,\mathrm{kV}$. With exposure time on the camera set to 1 s and gain set to 198, 300 frames were taken. As for the MCP voltage characterization, the slit was opened no wider than 300 µm.

For dot extraction, the threshold algorithm detailed in section 4.2 was chosen with a threshold of 10% of the maximum value of each image. Wavelength conversion was performed following the calibration from equation (12) using data from equation (13). Dots falling outside the calibrated region were discarded. Histogram bins were taken to be 0.05 nm wide, aligning with the wavelength distance covered by one pixel $a_{\mathrm{nm,px}}$. The resulting spectrum is shown in figure 27. Various peaks are visible, the highest two being very close to 160 nm. For comparison, the spectrum of a D_2 lamp measured with the Andor Newton CCD camera in section 3.3 and displayed in full in figure 16, is scaled and overlayed.

The spectrum taken with the MCP exhibits a shift of around 1.2 nm compared to the one taken with the CCD. Datasheet values and previous measurements correspond more closely to the CCD measurement, indicating that the alignment of the spectrometer during the MCP measurement was likely imprecise [22, 37]. To further evaluate whether peaks are noise or indeed the structure of the individual D_2 molecular lines, overlapping spectra at different central resolutions could be taken.

Die approbierte gedruckte Originalversion dieser Diplomarbeit ist an der TU Wien Bibliothek verfügbar
The approved original version of this thesis is available in print at TU Wien Bibliothek.

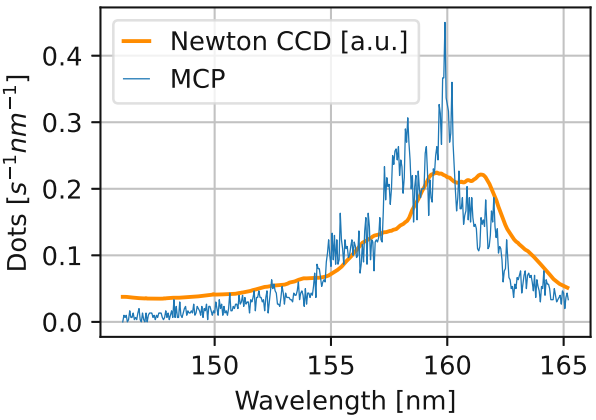

Figure 27: Spectrum of a D_2 lamp taken with an MCP. The entrance slit was smaller than 300 µm. Calibration data from equation (13) was used for reference, and binning in 0.05 nm steps applied. A part of the measurement of figure 16 is presented as well for comparison.

5 Reference light source for low-intensity VUV light

Light sources currently available for the VUV spectrum have low intensities compared to light sources for the visible spectrum but high intensity when compared to the expected photon output of ^{229m}Th experiments [22, 42]. However, weak, low-output light sources are needed for calibration, testing and development of ^{229m}Th experiments.

To complicate things further, these conventional VUV light sources are bulky, sometimes hard to operate and require special positioning far away from the slit. The positioning and distance of the light source in front of the slit can have a significant impact on the measured spectrum, as known by experience. This introduces uncertainty in the experiment and complexity in the analysis. Hence, a light source that can be installed as close as possible to the probed crystal is desirable.

Furthermore, sharp and stable reference lines in the vicinity of the expected ^{229m}Th line are needed as reference. Only few of the available options for VUV light sources fulfill this criterion.

No light source meeting these requirements was found. So out of necessity the idea of a new type of VUV reference light source was born. The concept involves a radioactive α-emitter that would serve as ionization source in a Xe environment in order to excite the 147 nm [1] atomic transition of elementary Xe. The result would be a small chamber with a weak but detectable sharp Xe peak that is easy to position and handle.

5.1 1st attempt: Puck attempt with 5 kBq source

A possible use case for such a light source was immediate as a beam time at ISOLDE (Isotope Separator On Line Device facility) of another group was approaching. For this reason, the very first attempt was made by the group and already designed to be usable if working.

For the mentioned first attempt at such a light source, aluminum disks with a 1 in diameter and 3 mm height were used as a starting point. After thorough cleaning and baking out, a 2 mm deep and 17 mm wide hole was drilled along the rotation axis. A ^{241}Am strip of around 7 mm length was extracted from a smoke detector and glued into the side of the hole using Torr Seal®. Then, a standard 1 in CaF_2 window was glued on top, again using Torr Seal®. During the gluing process, three hollow needles were left perforating the glue.

Once the glue was dried, a gas tent was filled with a little more than 1 bar of Xe. In the tent, a syringe was then filled with Xe and the gas injected through one of the hollow needles. This procedure was repeated multiple times. Then, the hollow needles were taken out and the remaining holes sealed with Torr Seal®. All of these steps were performed under Xe atmosphere and carried out by different members of the group. To speed up the hardening of the glue, the pucks were gently heated.

Using the CCD camera on the spectrometer and the grating at 0th order, no signal at all

Die approbierte gedruckte Originalversion dieser Diplomarbeit ist an der TU Wien Bibliothek verfügbar
The approved original version of this thesis is available in print at TU Wien Bibliothek.
TU Bibliothek Your knowledge hub WIEN

could be detected on a 14-hour measurement. Since a multitude of factors are possible reasons for the lack of signal, a more fundamental, step-by-step approach is needed to verify the concept.

5.2 2nd attempt: 33 kBq source, vessel filled with Kr

For a second attempt, the entire vacuum vessel was filled with noble gas and the radioactive source places right in front of the slit. That way, measurement at different pressures and with different gases became possible. However, it was only possible to use the CCD camera in this setup, and cooling of the camera was limited by the thermal conductivity of the gas filling.

As a replacement for the more expensive Xe gas, Kr was used. Krypton has a very strong atomic line at 123 nm [1] that we hoped to detect.

To further improve potential signal strength, the radioactive source was changed as well. Again, the source was extracted from an old smoke detector, this time shaped cylindrical and with an activity of 33 kBq of ^{241}Am. It was taped on the blind flange pointing upwards, that is, in the positive z direction. That way, α-particles emitted fly by the slit before hitting the upper wall of the grating chamber.

Measurements of the 0$^{\text{th}}$ order with the CCD camera exposing for 10 min with $1.4{\cdot}10^{-4}$ mbar, 5 mbar, 15 mbar, 50 mbar and 100 mbar of Kr did not show any signal.

However, at 250 mbar of Kr, a very weak signal could be seen by eye. A long measurement consisting of 14 frames with each 30 min exposure time was performed to improve statistics. Due to the pressure, the camera could only be cooled to −53 °C. To minimize readout noise, 4x4 binning was used. The highest 3% of pixel values were discarded as hot pixels and the median of all taken frames was formed. The measurement at 15 mbar was used as a reference to remove background. The resulting image is shown in figure 28a. To rule out any artifacts on the chip, the grating was rotated slightly and another measurement with 2 frames each exposed for 10 min with the camera cooled to −50 °C was taken. The resulting image after removing hot pixels, taking the of both images and scaling to improve visibility of the features is shown in figure 28b.

To show that the peak has moved, the column-wise mean is taken and brought into standardized form. The resulting graph is shown in figure 28c. Attempts to spectrally resolve the detected light using the CCD camera failed however, showing no detectable signal at all.

While this experiment showed that it is in principle possible to produce light using noble gases and an α emitter, yet another setup is necessary to further develop this technique and characterize the emitted light.

5.3 3rd attempt: Separate gas vessel

An experimental setup using a separate gas vessel would allow us to use a more sensitive detector, namely an MCP. Furthermore, the noble gas cannot reabsorb any light coming from atomic transitions. Since the volume of the gas vessel is smaller, more expensive gases or mixtures of gases can also be tried quickly.

These advantages led to the construction of a setup using a double-sided VUV-grade MgF_2 window. For such a setup, the window needs to be as close to the slit as possible to maximize signal. Therefore, a special ISO-K DN63 to CF DN40 adapter was made out of a ISO-K DN63 blind flange. The commercially available MgF_2 window furthermore had to be adjusted to fit M6 screws at a smaller diameter to not perforate the adapter and withstand the required mounting torques.

Special care was taken to position the α source at optimum distance for maximal signal. For that, the stopping distance of the emitted α particles needs to be calculated. The used source was, as before, a 33 kBq ^{241}Am cylinder, emitting α particles with an energy of 5.4 MeV.

Die approbierte gedruckte Originalversion dieser Diplomarbeit ist an der TU Wien Bibliothek verfügbar
The approved original version of this thesis is available in print at TU Wien Bibliothek.
TU Bibliothek Your knowledge hub WIEN

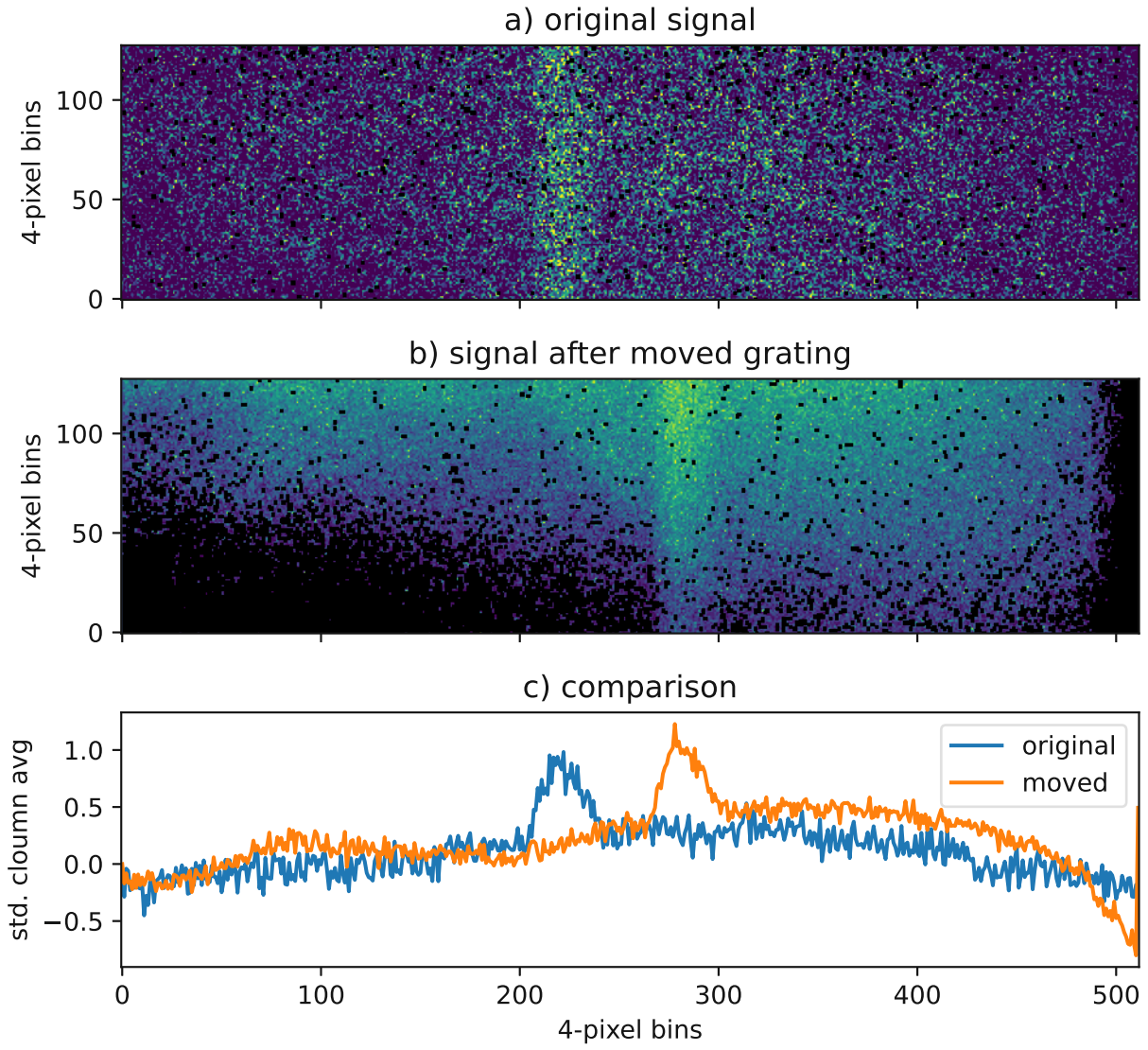

Figure 28: Original signal emitted by the ^{241}Am radioactive source as seen with a CCD camera at 0^{th} order (a), repeated measurement with slightly rotated grating but still at 0^{th} order (b) and comparison between both (c). For comparison, the column-wise mean was brought into standardized form. The peak moved, thereby confirming that the signal indeed came from the source and was not an artifact of the camera.

Die approbierte gedruckte Originalversion dieser Diplomarbeit ist an der TU Wien Bibliothek verfügbar
The approved original version of this thesis is available in print at TU Wien Bibliothek.

The decay chain essentially stops there as the daughter ^{237}Np has a half-life of 2.1 million years [40]. The energy loss over distance of particles can be described using the Bethe-Bloch equation. Unfortunately for us though, this equation only works poorly in the low-energy limit and with noble gases, making the calculation complex. For a variety of materials, calculations enhanced with experimental data can be retrieved from the NIST (National Institute of Standards and Technology) ASTAR database [3].

From previous experiments we know that 250 mbar of Kr should produce detectable amounts of light, as seen in figure 28. It is therefore reasonable to assume 250 mbar of Kr for a first estimate of where to position the source. Calculating the density of Kr at 250 mbar using

$$\rho = \frac{A_r p}{k_B T} \tag{14}$$

to be 0.86 kg/m^3, and using the value of the continuous slowing down approximation (CDSA) for Kr for α particles of 5.4 MeV from ASTAR, $1.149 \cdot 10^{-2}$ g/cm^2 [3], we get an expected range of 13.3 cm. The source was therefore positioned at a distance of around 13 cm away from the window.

This calculation neglects any losses before leaving the source as well as the detour taken by α particles due to scattering (which is very small) [3] and hence only describes the maximum distance α particles might travel before being stopped.

These considerations led to the creation of a setup with a separate gas vessel. Both vessels can be pumped separately. Standard Swagelock parts can be connected to the gas vessel. A schematic drawing of the setup is shown in figure 29.

Further measurements were then performed using an MCP detector instead of the CCD camera to achieve lower detection thresholds as signal rates are expected to drop with additional distance. Ideally, this would also allow us to spectrally resolve the light.

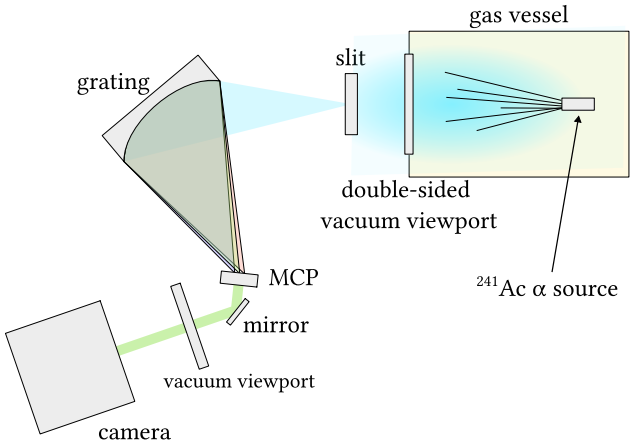

Figure 29: Schematic drawing of a separate gas vessel connected via a two-sided MgF_2 viewport to the main chamber. The α-particles excite noble gas atoms which then emit light isotropicly. Only a small fraction of the light enters the spectrometer.

Attempts to replicate the light that was seen in the previous attempt in section 5.2 using 250 mbar of Kr failed and no significant signal above the dark noise of the MCP could be seen.

Filling the chamber with Xe however immediately showed a clear signal at 0$^{\text{th}}$ order. The signal rate was not constant but decayed over time. A measurement was attempted to evaluate the time dependence of the signal, using the MCP on maximum voltage rating. This proved too intense to calculate positions of individual pixels, so the total signal area in pixels was taken as comparative quantity. Measurements were taken more or less every 25 min with each taking 20 frames with an exposure time of 5 s each and 330 camera gain. The resulting signal area values were normalized to the mean of the first measurement. An exponential decay with

$$I(t) = c_0 \cdot e^{-t/c_1} \tag{15}$$

was assumed and fitted to the data points, resulting in the parameters

$$\begin{aligned} c_0 &= 0.97, \\ c_1 &= 488\,\text{min}. \end{aligned} \tag{16}$$

The measured data and fit are shown in figure 30. As can be seen, around 30% of signal was

Die approbierte gedruckte Originalversion dieser Diplomarbeit ist an der TU Wien Bibliothek verfügbar
The approved original version of this thesis is available in print at TU Wien Bibliothek.
TU Bibliothek Your knowledge hub WIEN

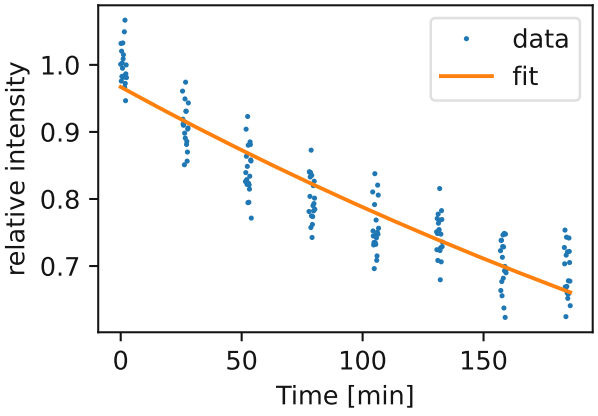

Figure 30: Time dependence of the Xe signal. Intensity was measured as total number of signal pixels on each frame. Frames were taken 20 at a time, with each 5 s exposure time and a gain of 330. The MCP was operated on maximum voltage rating. A exponential falloff is fitted through the data points.

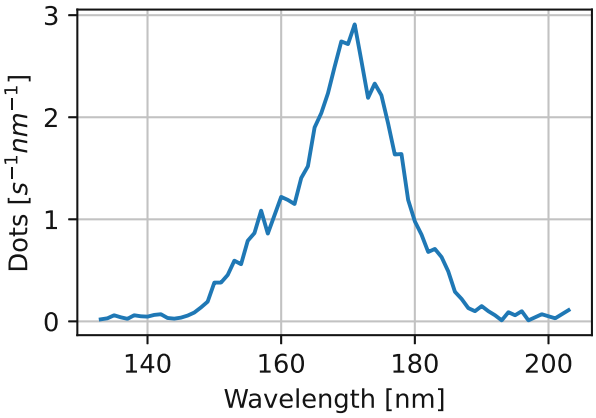

Figure 31: Spectrum of 321 mbar of Xe excited by a ^{241}Am α source, generated by combining 7 individual measurements on the MCP at different wavelengths. The underlying histogram was formed with 1 nm-sized bins.

lost after 3 hours measurement time. Likely reasons are that the gas vessel was not entirely airtight, thereby slowly leaking in air which might inhibit VUV light production.

The signal was intense enough for spectral analysis with the slit opened around 3 mm. A spectrum was taken by rotating the grating to seven different wavelengths at 145.3 nm, 150.0 nm, 152.5 nm, 167.2 nm, 175.0 nm, 181.9 nm and 199.0 nm. For each wavelength, 20 frames with an exposure time of 5 s were collected, using MCP supply voltages of $U_{\mathrm{MCPin}} = 1.375\,\mathrm{kV}$ and $U_{\mathrm{P}} = 3.5\,\mathrm{kV}$. Dots were extracted using the threshold algorithm detailed in section 4.2 with a threshold of 10%. Dot position to wavelength conversion was performed using equation (13). Dots were then collected in a histogram with 1 nm-spaced bins. The spectrum is shown in figure 31.

The observing reader might notice that this peak does not resemble to sought-after atomic transition line of Xe at all. Instead, a broad peak centering at 170 nm with a FWHM of 19.3 nm is visible, closely matching the characteristic excimer peak of Xe [2]. We can therefore safely conclude that the atomic transition is supressed in favor of the excimer process. One possible explanation is that the pressure of the gas is too high so that excimer formation is possible. Reducing the pressure might force excited atoms to de-excite directly and emitting the characteristic atomic spectrum. This might be helped by supplying a backing gas such as Argon at higher pressure which helps slow down α particles and transfer energy onto low-pressure Xenon.

A similar albeit less comprehensive measurement at a Xenon pressure of 147.8 mbar also showed a peak around 170 nm and only a tail at 147 nm. The reason why no signal at all was observed at similar pressures of Kr remains unclear.

As known by experience from Excitech excimer light sources, even very small contaminations of Xe in a Kr lamp produce atomic Xenon lines with significant intensity. A similar approach was tried as well, backing 100 mbar of Xe with 750 mbar of Ar. During filling with Argon, the corresponding excimer peak at around 135 nm was visible on the MCP. After filling the Xenon however the peak disappeared and

Die approbierte gedruckte Originalversion dieser Diplomarbeit ist an der TU Wien Bibliothek verfügbar
The approved original version of this thesis is available in print at TU Wien Bibliothek.
TU Bibliothek Your knowledge hub WIEN

the Xenon excimer peak appeared. A second attempt to reproduce the Argon excimer spectrum failed.

Summarizing, it was shown that noble gas excitation using a α source is feasible and leads to detectable light output. However, only the excimer spectrum could be produced so far, leaving the quest for excitation of the atomic transitions open.

6 Improvements to a scanning monochromator setup

The H+P spectrometer characterized in this work is not the only spectral apparatus in the group. Another one is used in a very different configuration to measure VUV transmission properties of samples. Dubbed the "Felixometer", it consists of a Hamamatsu D_2 lamp, a McPherson 302 vacuum vessel and grating holder, a sample holder and a solar-blind readout PMT [37] [2, sec. 4.2.1]. The setup is heavily used by the group for absorption measurements of doped CaF_2 crystals. Over time, various shortcomings have been identified and some work has been done to correct for them.

6.1 Intensity testing functionality

The sample holder consists of a wheel with 5 slots. Position is selected using a selection wheel with notches at the respective positions. A spring then presses a shaft into the notch, indicating to the user that the desired position has been reached. Unfortunately, these notches are not precise enough to reliably reproduce the exact position. Different positions in turn lead to different intensities measured on the PMT as different parts of the light and the probe are selected. Different intensities further lead to false results as the sample holder needs to be rotated between reference measurement and probe measurement.

To mitigate the problem, the spring locking into position was removed by the group. For each measurement, the position of the sample wheel is selected to maximize the intensity. That way, the measurements become reproducible again, positioning the sample wheel in such a way that a maximum of light passes through the probe.

The software controlling the setup was adapted to the new operating mode. An intensity test program flow was added, allowing to see currently measured values without exiting the program, thereby streamlining the workflow.

6.2 Driving the PMT in current mode

Originally, a Becker & Hickl counting card was used to detect photon pulses on the PMT output. An investigation into inconsistent behavior of the count rates showed reflections on one of the connectors used in the cabling of the PMT signal line.

Since the D_2 lamp focused onto the entrance slit provided plenty of signal, we did not replace the connector but instead started using the PMT in current mode. Instead of counting individual voltage peaks on the signal line, a current meter was connected and the current measured. As long as enough signal is available, driving the PMT in current mode yields good results, independent to reflections along the line [21].

As a current meter, a Keithley 2400 SourceMeter was deployed. It can be remotely controlled using its serial port. A python [11, 34] module was written for control and readout, and integrated into the existing measurement software[1]. The original software remains installed side-by-side so that the counting card can be used again if needed.

This modification not only resulted in more reliable readings but also faster measurement times as the current is already averaged so only

[1] On another note, since all parts of the transmission setup are now controlled via serial connections, the software can now run entirely on Linux as well.

Die approbierte gedruckte Originalversion dieser Diplomarbeit ist an der TU Wien Bibliothek verfügbar
The approved original version of this thesis is available in print at TU Wien Bibliothek.
TU Bibliothek Your knowledge hub WIEN

one measurement per wavelength needs to be taken.

7 Conclusion

A simultaneous spectrometer, or spectrograph, was built and characterized in multiple stages.

In a first stage, a camera with a rectangular CCD chip was mounted and aligned. Rough alignment was done using a laser while fine-tuning was performed by optimizing the width of the 121.5 nm line of a D_2 lamp. A FWHM of the line of 0.56 nm was achieved, indicating sub-nm resolution.

Using an Excitech E-Lux 147 excimer lamp with known contaminations, a wavelength to pixel relationship was established on both the rectangular, 1024×1024 pixel CCD chip and another wide-range 2048×512 CCD were calculated in section 3.2. It was shown that the spectrometer provides an almost linear pixel-wavelength relation for both the smaller and wider CCD, amounting to 0.0415 nm/px for the rectangular CCD and 0.0438 nm/px. Taking the size of the pixels into account, this amounts to a wavelength spacing in the focal plane of 0.0032 nm/mm.

Spectra of the D_2 lamp were taken with both CCDs in section 3.3, applying the wavelength-pixel relationship established before. Both spectra were found to align well with each other and the datasheet values of the lamp.

After the CCDs were characterized, the MCP and CMOS camera were installed. Vacuum problems were fixed as good as possible, reaching pressures of around $3.0 \cdot 10^{-6}$ mbar. Even if non-ideal, this pressure was good enough to allow operation of the MCP.

Special care was taken to understand and analyze the signal chain in order to find suitable processing and extraction steps. In the process, tools to verify results obtained from different algorithms were developed as well. Lacking the wide range of the CCD camera to image different peaks over a broad spectral region, wavelength-pixel relationship for the MCP & CMOS camera setup was found by rotating the grating to different wavelengths and recording their positions on the camera, leading to a conversion factor of 0.005 97 nm/px, as denoted in equation (13).

By using pinholes and filters, a D_2 lamp was sufficiently reduced in intensity to act as a light source for the MCP without immediately saturating the readout chain.

Different signal to noise ratios were found by scanning a large range of different supply voltages to the MCP assembly, shown in figure 26. However, measurement results were partly tainted due to fluctuations in lamp intensity. Still, three suitable regions with particularly high SNR were identified:

1. $U_{\mathrm{MCPin}} = 1.8\,\mathrm{kV}, U_{\mathrm{P}} = 1\,\mathrm{kV}$,
2. $U_{\mathrm{MCPin}} = 1.6\,\mathrm{kV}, U_{\mathrm{P}} = 2.5\,\mathrm{kV}$,
3. $U_{\mathrm{MCPin}} = 1.4\,\mathrm{kV}, U_{\mathrm{P}} = 3.5\,\mathrm{kV}$.

In contrast to measurements in literature, a dependency of dark counts to supply voltage was found, with dark counts decreasing as voltage decreases.

Intensity distributions of dots from dark and signal measurements were compared, indicating that dark counts tend to be more intense but only if no signal is impinging on the MCP.

Furthermore, a D_2 lamp spectrum in the 160 nm region was recorded, indicating sub-nm resolution.

In parallel to the characterization of the spectrometer, attempts to create a portable low-intensity, high-resolution VUV reference light source were made (section 5). For this endeavor, old smoke detectors were scavenged for ^{241}Am α particle sources. A first quick attempt using an aluminum puck filled with Xenon gas and a 5 kBq ^{241}Am strip and a CaF_2 window did not produce detectable results. However, in a second attempt the spectrometer chamber was entirely filled with 250 mbar of Kr and a more active, 33 kBq source, signal clearly emitted at the position of the source was identified.

In a third, more sophisticated attempt, this result using Kr was not reproduced. Instead,

Die approbierte gedruckte Originalversion dieser Diplomarbeit ist an der TU Wien Bibliothek verfügbar
The approved original version of this thesis is available in print at TU Wien Bibliothek.
TU Bibliothek Your knowledge hub WIEN

however, signal could be seen with 321 mbar of Xe, and a spectrum was taken. The spectrum is shown in figure 31, and shows the characteristic eximer spectrum instead of the desired sharp line at 147 nm. Additionally, the signal decayed over the course of hours, likely due to contaminations entering the system. Attempts to use a mixture of gases similar to the excimer lamps to stimulate the atomic Xe lines gave no results.

Last but not least, optimizations to the scanning monochromator used for transmission measurements were made (section 6). To improve the workflow with the device, an intensity test mode was implemented, making it possible to manually optimize the rotation of the sample holder so that signal reaches a maximum. This improves reproducibility of the measurements as the sample holder lacks precise positioning capabilities. In addition, the turn from pulse counting to current measurement was made on the PMT readout. This is possible because of the high count rates, and ultimately, because of the intense D_2 lamp employed.

7.1 Outlook

The installation and characterization of the VUV spectrograph provide some fundamental understanding of the setup. Hence, the present thesis can serve as a basis for further analysis and experiments.

One hot topic that remains after this work is the analysis of images containing dots. Different schemes showed promise and it is of interest to quantify how well they work. For that, a manually classified dataset covering a number of cases could be created and algorithms benchmarked against it.

The noise characteristics and the thermal behavior of the CMOS camera are another interesting topic as they could allow the classification of dots based on their height as well, or operation and characterization of the MCP at even lower voltages. One potential use case would be the rejection of high-energy events.

In literature, dot intensities are often given in pulse height distributions. Finding a conversion factor between dot intensities and pulse heights could help use synergies from other research, for example regarding the noise characteristics.

While wavelength to pixel relationships were established for both CCDs and a specific setup of MCP and CMOS camera, the resolution of the MCP still remains widely unstudied even tough tools to estimate the resolution from the spectrum are available [2, 28].

Most importantly, the setup is to be used in the direct detection of the ^{229m}Th isomer. With a proper calibration source, proper choice of parameters and proper data analysis, this setup has been proven to be up for the task of delivering the potentially most precise measurement of the isomer's energy to date.

References

[1] A. Kramida et al. *NIST Atomic Spectra Database*. Version 5.9. National Institute of Standards and Technology, Gaithersburg, MD, 2021. DOI: 10.18434/T4W30F. (Visited on 2022-06-06).

[2] Kjeld Adrianus Antonius Gerardus Beeks. "The Nuclear Excitation of Thorium-229 in the CaF2 Environment". eng. PhD thesis. Wien: TU Wien, 2022. DOI: 10.34726/hss.2022.99008.

[3] M.J. Berger et al. *ESTAR, PSTAR, and ASTAR: Computer Programs for Calculating Stopping-Power and Range Tables for Electrons, Protons, and Helium Ions*. Version 2.0.1. National Institute of Standards and Technology, Gaithersburg, MD, 2017. DOI: 10.18434/T4NC7P. (Visited on 2022-06-06).

[4] Tobias Bothwell et al. "Resolving the gravitational redshift across a millimetre-scale atomic sample". eng. In: *Nature (London)* 602.7897 (2022), pp. 420–424. ISSN: 0028-0836. DOI: 10.1038/s41586-021-04349-7.

[5] E. Browne and J.K. Tuli. "Nuclear Data Sheets for A = 229". In: *Nuclear Data Sheets* 109.11 (2008), pp. 2657–2724. ISSN: 0090-3752. DOI: 10.1016/j.nds.2008.10.001.

Die approbierte gedruckte Originalversion dieser Diplomarbeit ist an der TU Wien Bibliothek verfügbar
The approved original version of this thesis is available in print at TU Wien Bibliothek.
TU Bibliothek Your knowledge hub WIEN

[6] L. R. P. Butler and K. Laqua. "Nomenclature, symbols, units and their usage in spectrochemical analysis-IX. Instrumentation for the spectral dispersion and isolation of optical radiation (IUPAC Recommendations 1995)". In: *Pure and Applied Chemistry* 67.10 (1995), pp. 1725–1744. DOI: 10.1351/pac199567101725.

[7] Bhaskar Choubey, Waqas Mughal, and Luiz Gouveia. "CMOS circuits for high-performance imaging". In: *High Performance Silicon Imaging (Second Edition)*. Ed. by Daniel Durini. Second Edition. Woodhead Publishing Series in Electronic and Optical Materials. Woodhead Publishing, 2020, pp. 119–160. ISBN: 978-0-08-102434-8. DOI: 10.1016/B978-0-08-102434-8.00005-2. URL: https://www.sciencedirect.com/science/article/pii/B9780081024348000052.

[8] D. Durini and D. Arutinov. "1 - Fundamental principles of photosensing". In: *High Performance Silicon Imaging*. Ed. by Daniel Durini. Second Edition. Woodhead Publishing Series in Electronic and Optical Materials. Woodhead Publishing, 2020, pp. 3–24. ISBN: 978-0-08-102434-8. DOI: 10.1016/B978-0-08-102434-8.00001-5.

[9] Edward H. Eberhardt. "Gain model for microchannel plates". In: *Appl. Opt.* 18.9 (May 1979), pp. 1418–1423. DOI: 10.1364/AO.18.001418.

[10] Inc. Edmund Optics. *Compact Fixed Focal Length Lens #59-872*. URL: https://www.edmundoptics.com/document/download/380180 (visited on 2022-06-23).

[11] Python Software Foundation. *Python*. Version 3.10. June 6, 2022. URL: https://docs.python.org/3/.

[12] G.W. Fraser, J.F. Pearson, and J.E. Lees. "Dark noise in microchannel plate X-ray detectors". In: *Nuclear Instruments and Methods in Physics Research Section A: Accelerators, Spectrometers, Detectors and Associated Equipment* 254.2 (1987), pp. 447–462. ISSN: 0168-9002. DOI: 10.1016/0168-9002(87)90699-1.

[13] excitech GmbH. *E-Lux light source specifications*. URL: http://excitech.de/ELux_excitech.pdf (visited on 2022-06-23).

[14] GIDS GmbH. *Phosphor Screens and Scintillators Datasheet*. 2015. URL: https://gids-gmbh.com/wp-content/uploads/2020/02/Phosphor-Screens.pdf (visited on 2022-06-27).

[15] H+P Spectroscopy GmbH. *EasyLIGHT 1076 Manual*. 2020.

[16] H+P Spectroscopy GmbH. *easyLIGHT VUV Spectrometer*. Mannheim, Germany. URL: https://www.hp-spectroscopy.com/_files/ugd/318e38_16ef670a28884178a412b706bd7c5177.pdf (visited on 2022-06-23).

[17] ProxiVision GmbH. *Phosphor Screens Datasheet*. URL: https://www.proxivision.de/datasheets/Phosphor-Screen-PR-0056E-03.pdf (visited on 2022-06-27).

[18] A S Jursa. *Handbook of Geophysics and the Space Environment. 4th edition*. Dec. 1985. URL: http://www.cnofs.org/Handbook_of_Geophysics_1985/pdf_menu.htm (visited on 2021-05-25).

[19] Hamamatsu Photonics K. K. *Final Test Sheet for F3490-21P-Y006*. 2021.

[20] Hamamatsu Photonics K. K. *MCP Assembly F3490 Technical Drawing AF3490-A064A*. 2020.

[21] Hamamatsu Photonics K. K. *Photomultiplier Tubes - Basics and Applications*. Fourth Edition. 2017. URL: https://www.hamamatsu.com/content/dam/hamamatsu-photonics/sites/documents/99_SALES_LIBRARY/etd/PMT_handbook_v4E.pdf (visited on 2022-06-26).

[22] Hamamatsu Photonics K.K. *Deuterium lamp L11798*. URL: https://www.hamamatsu.com/resources/pdf/etd/L11798_L11799_TLSZ1014E.pdf (visited on 2021-05-14).

Die approbierte gedruckte Originalversion dieser Diplomarbeit ist an der TU Wien Bibliothek verfügbar
The approved original version of this thesis is available in print at TU Wien Bibliothek.

[23] N. Kawai and S. Kawahito. "Noise analysis of high-gain, low-noise column readout circuits for CMOS image sensors". In: *IEEE Transactions on Electron Devices* 51.2 (2004), pp. 185–194. DOI: 10.1109/TED.2003.822224.

[24] Masato Koike. "Normal Incidence Monochromators and Spectrometers". In: *Vacuum Ultraviolet Spectroscopy*. Ed. by J.A.R. Samson and D.L. Ederer. Burlington: Academic Press, 1999, pp. 1–20. ISBN: 978-0-12-617560-8. DOI: 10.1016/B978-012617560-8/50023-2.

[25] A. Lahav et al. "Backside illuminated (BSI) complementary metal-oxide-semiconductor (CMOS) image sensors". In: *High Performance Silicon Imaging (Second Edition)*. Ed. by Daniel Durini. Second Edition. Woodhead Publishing Series in Electronic and Optical Materials. Woodhead Publishing, 2020, pp. 95–117. ISBN: 978-0-08-102434-8. DOI: 10.1016/B978-0-08-102434-8.00004-0.

[26] M. Lesser. "Charge-coupled device (CCD) image sensors". In: *High Performance Silicon Imaging*. Ed. by Daniel Durini. Second Edition. Woodhead Publishing Series in Electronic and Optical Materials. Woodhead Publishing, 2020, pp. 75–93. ISBN: 978-0-08-102434-8. DOI: 10.1016/B978-0-08-102434-8.00003-9.

[27] e2v technologies limited. *CCD42-10 Back Illuminated High Performance AIMO CCD Sensor*. Version A1A-100024 Version 10. 2016. URL: https://www.teledyneimaging.com/download/38b4bc3f-1448-4668-9ab6-ae61c15867af/ (visited on 2022-06-23).

[28] M. Mallweger. "Deuteriumlamp as a calibration source for a superconducting nanowire". project thesis. Technical University of Vienna. 2020. unpublished.

[29] S. Matsuura et al. "Characteristics of the Newly Developed MCP and Its Assembly". In: *IEEE Transactions on Nuclear Science* 32.1 (1985), pp. 350–354. DOI: 10.1109/TNS.1985.4336854.

[30] Inc. McPherson and AinnoTech. *McPherson Model 234/302 Spec Sheet*. URL: http://ainnotech.com/ainnotech/pdf/06/2_1/5MC-234%20302-0.2%20meter%20focal%20length%20vacuum%20scanning%20spectrometer.pdf (visited on 2022-06-24).

[31] Zachary L. Newman et al. "Architecture for the photonic integration of an optical atomic clock". In: *Optica* 6.5 (May 2019), pp. 680–685. DOI: 10.1364/OPTICA.6.000680.

[32] Oxford Instruments plc. *Andor iKon-M 934 DO/SO Series Specs*. Version XIKONM934DOSS 0311 R1. Tubney Woods, Abingdon, Oxon OX13 5QX, UK.

[33] Oxford Instruments plc. *Andor Newton SO Series Specs*. Version XIKONM934DOSS 0311 R1. Tubney Woods, Abingdon, Oxon OX13 5QX, UK. URL: https://andor.oxinst.com/assets/uploads/products/andor/documents/andor-newton-so-specifications.pdf (visited on 2022-06-23).

[34] *pyserial*. Version 3.5. June 6, 2022. URL: https://pythonhosted.org/pyserial/.

[35] QHYCCD. *Setting GAIN and OFFSET on cold CMOS camera for deep sky astrophotography*. 2018. URL: https://www.qhyccd.com/uploadfile/2018/1106/20181106030334403.pdf (visited on 2022-06-26).

[36] G. W. Rubloff. "Far-Ultraviolet Reflectance Spectra and the Electronic Structure of Ionic Crystals". In: *Phys. Rev. B* 5 (2 Jan. 1972), pp. 662–684. DOI: 10.1103/PhysRevB.5.662.

[37] F. Schneider. "Scanning monochromator for the Vacuum Ultraviolet wavelength range". project thesis. Technical University of Vienna. 2021. unpublished.

[38] S. Shionoya, W.M. Yen, and H. Yamamoto, eds. *Phosphor Handbook*. eng. Second Edition. CRC Press, 2007. DOI: 10.1201/9781315222066.

Die approbierte gedruckte Originalversion dieser Diplomarbeit ist an der TU Wien Bibliothek verfügbar
The approved original version of this thesis is available in print at TU Wien Bibliothek.
TU Bibliothek Your knowledge hub WIEN

[39] Tomas Sikorsky et al. “Measurement of the ^{229}Th Isomer Energy with a Magnetic Microcalorimeter”. In: *Physical Review Letters* 125.14 (Sept. 2020). ISSN: 1079-7114. DOI: 10.1103/physrevlett.125.142503.

[40] Sóti, Zsolt, Magill, Joseph, and Dreher, Raymond. “Karlsruhe Nuclide Chart 10th edition 2018 ”. In: *EPJ Nuclear Sci. Technol.* 5 (2019), p. 6. DOI: 10.1051/epjn/2019004.

[41] Inc Stanford Computer Optics. *Image intensifier: Phosphor screen.* URL: https://stanfordcomputeroptics.com/technology/image-intensifier/phosphor-screen.html (visited on 2022-06-27).

[42] Simon Stellmer et al. “Feasibility study of measuring the ^{229}Th nuclear isomer transition with ^{233}U-doped crystals”. In: *Phys. Rev. C* 94 (1 July 2016), p. 014302. DOI: 10.1103/PhysRevC.94.014302.

[43] Nikolai V. Tkachenko. “Chapter 2 - Optics and Optical Devices”. In: *Optical Spectroscopy*. Ed. by Nikolai V. Tkachenko. Amsterdam: Elsevier Science, 2006, pp. 15–38. ISBN: 978-0-444-52126-2. DOI: 10.1016/B978-044452126-2/50026-5.

[44] M. Verlinde et al. “Alternative approach to populate and study the ^{229}Th nuclear clock isomer”. In: *Phys. Rev. C* 100 (2 Aug. 2019), p. 024315. DOI: 10.1103/PhysRevC.100.024315.

[45] Pierre Villars and Karin Cenzual, eds. *CaF2 Crystal Structure: Datasheet from “PAULING FILE Multinaries Edition – 2012” in SpringerMaterials.* URL: https://materials.springer.com/isp/crystallographic/docs/sd_0378096 (visited on 2021-04-20).

[46] Pauli Virtanen et al. “SciPy 1.0: Fundamental Algorithms for Scientific Computing in Python”. In: *Nature Methods* 17 (2020), pp. 261–272. DOI: 10.1038/s41592-019-0686-2.

Die approbierte gedruckte Originalversion dieser Diplomarbeit ist an der TU Wien Bibliothek verfügbar
The approved original version of this thesis is available in print at TU Wien Bibliothek.